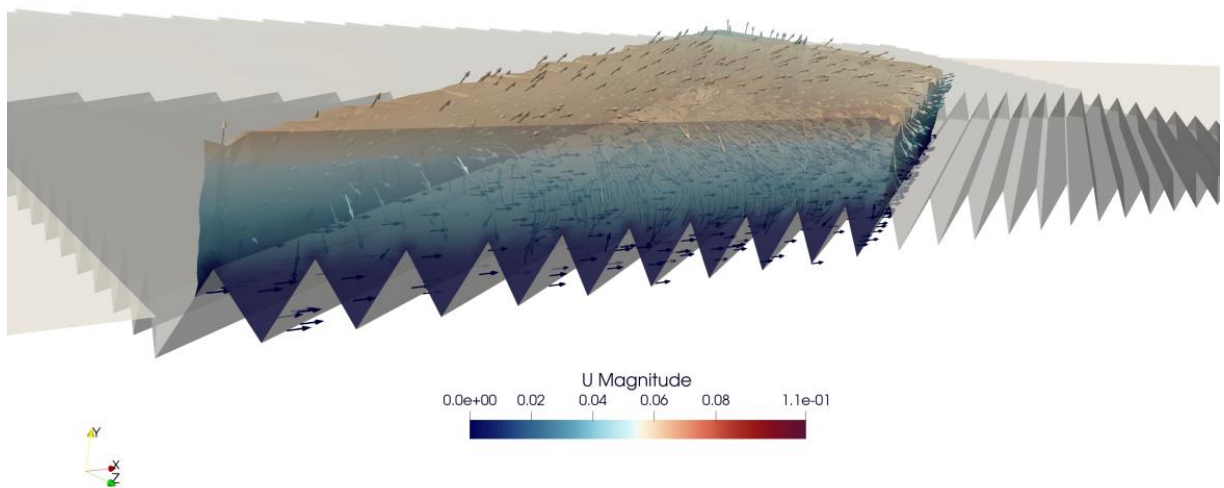# Evaluation of Parametric Effects of Micro-structural Riblets on the Boundary Layer Flow over Flat Plate

FOSSEE 2023 Summer Fellowship Report

ASHUTOSH KUMAR

Department Of Mechanical Engineering
BIRSA INSTITUTE OF TECHNOLOGY, SINDRI
DHANBAD, JHARKHAND

Evaluation of Parametric Effects of Micro-structural Riblets on the Boundary Layer Flow over Flat Plate

Submitted by

Ashutosh Kumar

Department of Mechanical Engineering
B.I.T. Sindri

Under the guidance of

Dr. Mrinal K R

Assistant Professor
Department of Mechanical Engineering
The National Institute of Engineering

Abstract

This study aims to realize the effect of riblets on the flow over a flat plate. The empirical relations developed for boundary layer flow over the flat plate can be used to approximate the flow parameters in various applications involving a viscous flow regime over an unbounded wall boundary. Different devices and techniques for manipulating the flow over flat plates have been developed. Riblets, which can be thought of as passive flow actuators, are inspired by the dendrites found in shark skins and the grooved structures in some birds. They have been found to reduce skin friction drag by a significant amount and are being tested for use in aircraft wings and empennage, turbo-machinery blades, automotive bodies, etc. In the current study, we aim to delve into the flow patterns in the boundary layer flow over a flat plate with riblet section and compare flow properties with base configuration of a flat plate. Also, the effect of variations in the yaw angles of the riblets has been studied. Since the flow regime in our study is laminar, a steady-state solver, **simpleFoam** was chosen for computation. Influence of riblet sections on turbulent flows have been vastly covered in the literature but there seems to be little research on the effects on laminar flow. In our investigation, we develop a methodology to investigate the effect of riblets on the secondary flow in the boundary layer over flat plate with riblet section and the effect of yaw configurations as well as Reynolds Numbers.

Contents

List of Figures

List of Tables

List of Tables

1

Introduction

In this study, the effect of convergent-divergent riblets on the flow over a flat plate is analyzed using numerical methods using and open-source software Open-Foam, which is a C++ toolbox developed to evaluate problems dealing with continuum mechanics computationally and has been extensively used in several industries and the academia for the same since its formulation. The primary objective of this report is to explore the effect of convergent-divergent riblets on the boundary layer flow over a flat plate and to investigate their potential for drag reduction and flow stabilization. The idea behind converging-diverging riblets is inspired by the natural structures found in the skin of certain species of sharks, which help reduce drag and improve swimming efficiency. Analysing these structures in details, it was verified that by controlling the boundary layer flow, these sharks are able to swim significantly fast with increased efficiency. By analyzing the flow behavior, we aim to gain insights into the underlying physical mechanisms governing the interaction between the riblet structures and the boundary layer flow. Also, we try to develop a comparison between the C-D riblets and the more conventional configurations of longitudinal and transverse riblets. In the present study, our focus lies specifically on convergent-divergent riblets and their influence on the flow characteristics over a flat plate. But this can be used as a platform for exploring other configurations which have been incorporated in the recent times. Convergent-divergent riblets represent an innovative departure from conventional straight riblets, boasting a unique geometry that imparts both converging and diverging features along their span. This distinctive configuration promises novel and possibly superior flow control mechanisms compared to traditional riblet patterns.

1.1 Motivation

Fluid flow is an integral aspect of many industrial processes. The ever-increasing quest to minimize energy consumption has led to the devising of innovative methods to reduce costs and conserve resources. One of which is bio-mimicry, or bio-inspired design, which essentially is the practice of studying, drawing inspiration from, and emulating nature's structures, processes, and strategies to solve human problems and create innovative solutions. The core idea behind bio-mimicry is that nature, through evolution, has already found practical solutions to many challenges living organisms face. By observing and understanding these natural designs and processes, scientists and engineers can apply the principles and strategies to create more sustainable, efficient, and resilient technologies and systems. Of the many that have

been researched over and developed in a working form in the past few decades is the design of micro-structural grooves that influence boundary layer flows. These structures can be thought of as passive flow controllers since they don't need any power source to function. Riblets are inspired by the fundamental design of the skin of sharks. Sharks have a unique skin texture with small, tooth-like structures called denticles. These denticles are microscopically small, V-shaped ridges or grooves that cover the shark's skin in a parallel pattern.
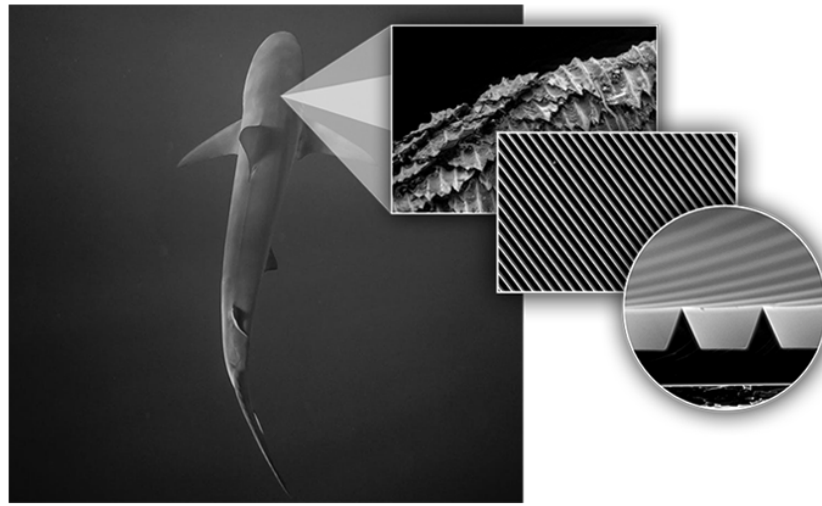
Figure 1.1: Grooved Structures present in shark skin

This can be accounted for the reason for the reasons sharks can swim fast through the water and the denticles have a role to play in reducing skin friction hence the swimming behavior is efficient.

The denticles on sharkskin help reduce drag as water flows over their bodies, allowing them to move more efficiently and with less resistance through the water. The idea of mimicking this natural design led to the development of artificial riblet patterns on various surfaces to achieve similar drag reduction benefits. The concept of drag-reducing riblets was first observed in the late 1960s and the applications of drag-reducing riblets can be found in various fields:

- Aerospace: Riblet technology has been used in aircraft design, particularly on wings and fuselage surfaces, to reduce aerodynamic drag and improve fuel efficiency.

- Marine: In shipbuilding, riblets on hulls and propellers can enhance hydrodynamic performance, reducing fuel consumption and increasing speed.

- Sports: Riblet textures have been applied to swimsuits, competitive swimsuits, and even the hulls of racing boats to decrease drag and improve performance.

- Wind turbines: Drag-reducing riblets on the blades of wind turbines can help increase energy efficiency by reducing resistance to the wind.
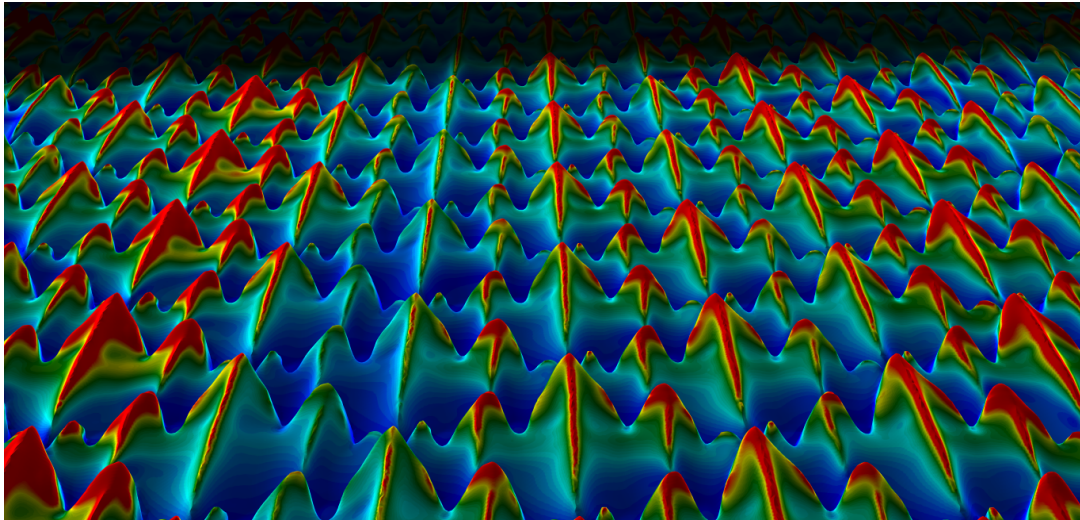
Figure 1.2: Flow pattern visualization over Shark Skin scales.

The primary benefit of drag-reducing riblets is their potential to improve energy efficiency and performance, which is especially crucial in industries where minimizing drag can lead to significant cost savings and environmental benefits. With the regulations concerning the usage of fuel as a driving source for most of transportation vehicles becoming more stringent than ever, it would be beneficial to incorporate drag-reducing mechanisms for better efficiency. Even when the power consumption is by battery packs, drag plays an important role in the overall range. Also, the overheating issue of battery packs can be reduced to some extent by reducing the fraction of power required to overcome the drag.

1.2 Objective

The objective of this study is to analyze how the convergent-divergent riblets affect the laminar boundary layer flow over a flat plate. The primary inspiration for using converging-diverging riblets comes from the observation of shark skin. Certain shark species have tiny scales called 'dermal denticles' that cover their skin. These denticles are riblet-like structures with a specific pattern. This pattern helps reduce the skin friction drag as water flows over the shark's body, allowing it to swim more efficiently. Experiments involving the incorporation of riblets for manipulating turbulent external as well as internal flows have been widely studied but not the same amount of exposure has been given to laminar flows.

- We delve into the characteristics of vortices developed over riblets and how these affect the overall behavior of boundary layer flow influencing the wall shear stress in near-wall regions.

The mechanism for drag reduction in turbulent flows owes to the fact that the span-wise velocity fluctuations are hampered and diminished by the presence of riblet tips. This in turn damps the momentum transfer across the spanwise direction reducing the overall turbulent skin friction.

- However the mechanism in laminar flows has to have a different physical principle since in laminar flows, the exchange and mixing between layers is not too profound. Therefore, we also try to examine how the process of redistribution of near-wall velocity gradients modifies the skin friction and how the generation of longitudinal vortex rolls can delay the boundary layer separation energizing the boundary layer in order to enable the fluid layer attached to the wall to traverse the adverse-pressure gradient.

The variation of intensity of roll motion and the velocity characteristics of the flow induced by yawed riblets over the plate are investigated.

Eventually, we establish the comparison between the effects of riblet yaws and how they effect the skin friction pattern not only in the section where riblets are installed but the region of flat plate that falls behind the end of the the riblet section.

2

Literature Review

2.1 Introduction

Drag reduction riblets have been under study and investigation since the early 1980s and drag reduction of up to 10 percent has been observed in experimental studies. A significant amount of drag reduction has been observed in both water and air as a medium. The additional benefit of using riblets is the overall size reduction of the flow control device that is in contact with fluid, i.e. wetted surface, as compared to conventional vortex generators, which tend to minimize the influence of these structures on the flow characteristics itself. Riblets also delay flow separation through a combination of mechanisms that alter the flow characteristics near the surface, specifically within the boundary layer :

1. **Influence on Shear Stress** : The fluid's velocity near the surface is zero due to the no-slip condition due to the wall surface. Moving away from the surface, velocity gradients develop, and the shear stress is a linear function of the wall-normal velocity gradient. Riblets affect the boundary layer's velocity gradient, altering the shear stress distribution.

2. **Flow Re-energization** : Riblets act as miniature vortex generators. The flow inside the riblet grooves induces small-scale vortices that re-energize the boundary layer. This re-energization helps to prevent the flow from transitioning into turbulent patterns.

3. **Maintaining the Laminar Flow** : By re-energizing the boundary layer and promoting small-scale vortices, riblets help to maintain laminar flow for a more extended period along the surface. Laminar flow has lower energy losses than turbulent flow, resulting in reduced drag.

The inspiration for incorporating these microstructural patterns was drawn from the instances of efficiency advantages in fast-swimming sharks and the secondary feathers of some birds. Apart from aerodynamic benefits, riblet structures in bird feathers also enable silent flight as a consequence of their passive flow control capabilities which induce small-scale vortex structures to break down the turbulent eddies and, thus, reduce the temporal acoustic pressure perturbations.

2.2 Drag Reduction Mechanism

According to Bechert et al.(1997), for the dimensionless riblet spacing length of $s^+ \approx 17$ and riblet spacing to riblet height ratio of $s/h \approx 2$, drag reduction of up to 10% was observed (where $s^+ = sU_\tau/\nu$ is the dimensionless riblet spacing; U_τ being the frictional velocity and ν the kinematic viscosity). The reasoning for this lies in the fact that the mean diameter of vortices is $d^+ \approx 30$ which is greater than the riblet spacing for up to $s^+ < 30$, and thus only the riblet tips are in contact with the vortices which reduces the skin friction as compared to smooth plates. A large portion of the total wetted surface area is in contact with the regions of insignificant velocity gradients and the fluid film trapped in the spaces between riblet tips is almost stationary. The second reason behind the effectiveness of riblets in reducing skin friction in turbulent flows is the interaction of riblet tips with the cross-flow. Bechert et al.(1997) also emphasized the fact that the origins of longitudinal flow and cross-flow don't coincide and the latter is much nearer to the tip of riblets.
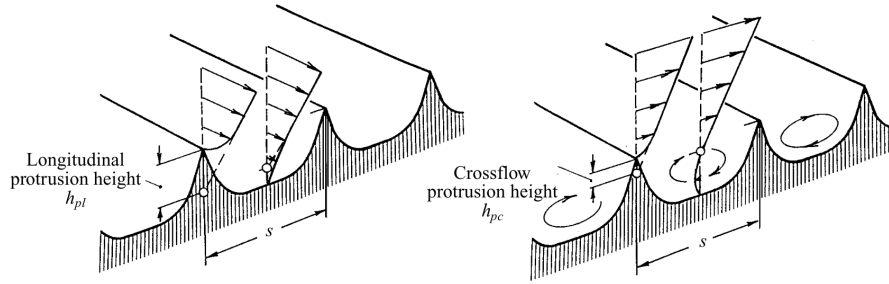
Figure 2.1: Longitudinal and Crossflow over Riblets

Thus the interaction between riblet tips and the crossflow is more profound. In turbulent flow interactions, the shear stress that is developed over a surface depends on velocity fluctuations apart from the wall-normal velocity gradients. The riblets lie in the viscous sublayer regime and play a part in manipulating the fluctuating velocity part of the crossflow w'.

The reduction in the magnitude of the fluctuating velocity component w' has a direct impact on momentum transport in cross-stream direction and therefore the turbulent shear stress is reduced. As is confirmed by direct numerical simulation (Choi,Moin and Kim 1993).

According to Frohnapfel et al.(2007), the anisotropic state of turbulence can be observed in the space between riblet edges which are a further cause of drag reduction (**Fig. (2.2)**). Lumley and Newman(1977) state that the degree of anisotropy present in the flow can be used to describe the turbulence state. By eliminating the isotropic portion from τ_{ij} and normalizing using $\tau_{ss} = -\rho\overline{u_s u_s}$, it is possible to calculate the degree of anisotropy of a flow from the Reynolds stresses $\tau_{ij} = -\rho\overline{u_i u_j}$.
Thus, the non-dimensional anisotropy can be written as:

$$a_{ij} = \frac{\overline{u_i u_j}}{2k} - \frac{1}{3}\delta_{ij} \tag{2.1}$$

where $k = \frac{1}{2}\overline{u_s u_s}$, and δ_{ij} is the Kronecker delta function.

The tensor a_{ij} has three scalar invariants:

$$a_{ij} = 0, \quad \text{II}_a = a_{ij}a_{ji}, \quad \text{III}_a = a_{ij}a_{jk}a_{ki} \tag{2.2}$$
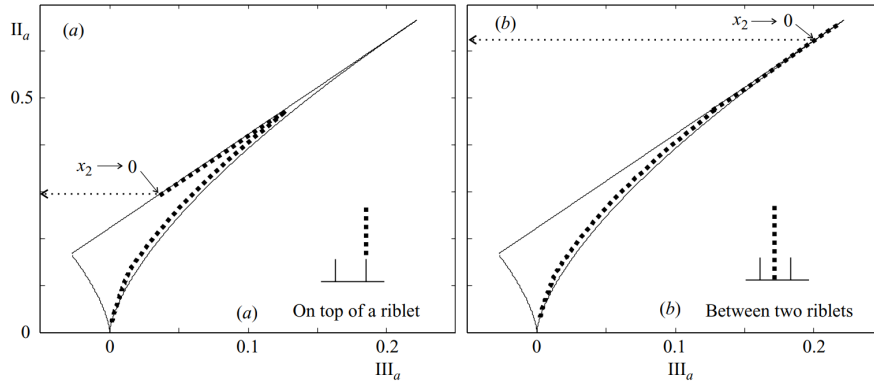
Figure 2.2: Anisotropy invariant plot for *(a) flow on riblet tip*, and *(b) flow in riblet spacing.*

A flow's turbulence condition in relation to anisotropy can be shown by cross-plotting II_a and III_a. Upon evaluating the scalar invariants II_a and III_a for the situation of a two-component turbulent flow (where one component of the velocity fluctuations is minuscule in comparison to the other two), this results in

$$\text{II}_a = \frac{2}{9} + 2\text{III}_a \tag{2.3}$$

Doing the same for the axisymmetric turbulence (two components are equal in magnitude) yields

$$\text{II}_a = \frac{3}{2}\left(\frac{4}{3}|\text{III}_a|\right)^{\frac{2}{3}} \tag{2.4}$$

The two equations (2.3) and (2.4) when plotted against each other represent what is called the **anisotropy invariant map** and in the **Fig.(2.2)**, it can be observed that The one-component turbulence is achieved in the case of flow between the riblets and the flow remains axisymmetrical otherwise in contrast to the flow on the riblet tip.

Grüneberger(2010) states that the viscous theory has two fundamental outcomes with respect to the drag reduction mechanism by riblets in the viscous sublayer

regime. The riblet geometry has a direct impact on both the longitudinal and cross-flow velocity distributions. Different velocity distributions over ribbed surfaces for longitudinal and cross-flow flow are connected to how well these surfaces reduce drag. The drag reduction of that riblet geometry is correlated to the distance between the origins of the velocity profiles for longitudinal and cross-flow.

2.3 Riblet Configurations

Different configurations of riblets have been experimented with varying yaw angles(γ), riblet spacing(s), and riblet height(h). The configuration with yaw angle $\gamma = 0^o$ in which the direction of freestream flow is aligned with riblet length is longitudinal riblets and the one with yaw angle $\gamma = 90^o$ having the freestream flow normal to the riblet section length direction is transverse riblets. On the basis of geometry, riblets sections can be of different forms, blade-shaped riblets, scalloped riblets, trapezoidal riblets, V-grooved riblets.
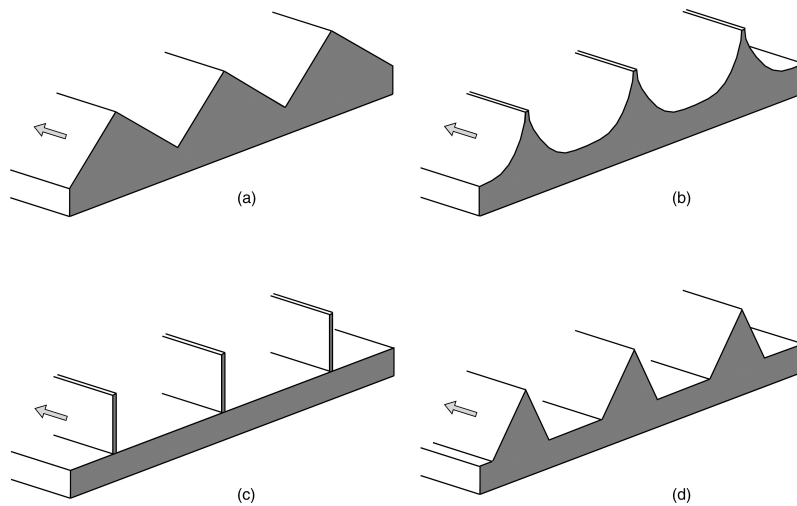
Figure 2.3: Riblet Geometry Configurations *(a) V-grooved Riblets, (b) Scalloped Riblets, (b)Blade Riblets*, and *(d) Trapezoidal Riblets*

Laboratory measurements from several studies were conducted (e.g. *Berchert et al. 1997, Walsh and Weinstein 1978, Walsh and Weinstein 1978, Lucchini et al. 1991*) to understand the relation between riblet parameters (like non-dimensional riblet spacing s^+, non-dimensional riblet height h^+, riblet shape) and their effects on reduction in wall shear stress. A review by Berchert et al. 1997 and Walsh 1990 suggested that there exists a common trend of drag reduction amongst riblets of all shapes with respect to the non-dimensional riblet spacing s^+ wherein, up to a certain value of s^+ drag reduction is observed until it reaches an optimum point. The drag reduction then starts diminishing in magnitude and the effect of riblets begins to reverse as s^+ increases. The riblet spacing s^+ of the configuration for which the maximum drag reduction was observed was found to be approximately 15. In the region where the non-linear effects on the flow close to the walls are substantially

low, i.e. the viscous region, the drag reduction metric **DR** is proportional to the normalized riblet spacing s^+.

Here, $\mathbf{DR} = \frac{\Delta\tau}{\tau_o} = \left(\frac{\tau - \tau_o}{\tau_o}\right)$; τ_o is the skin friction in the case of smooth flat plate, and τ is the skin friction with riblets.
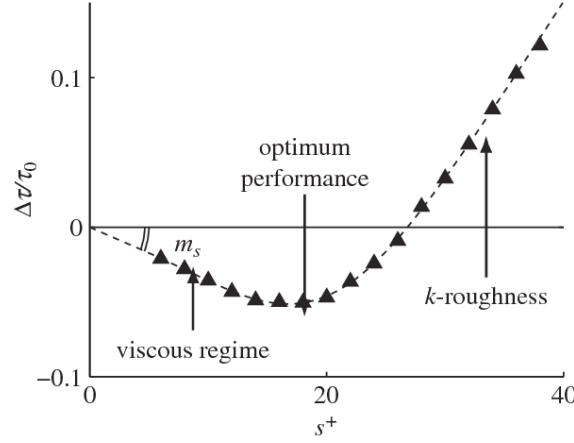
Figure 2.4: Relation between normalized riblet spacing s^+ and drag reduction

With the advent of the optimum range of normalized riblet spacing, $s^+ = s_{opt}^+$, the viscous regime decays (around $s^+ \approx 15$) before the reversal of drag reduction phenomenon in which the drag starts to increase.
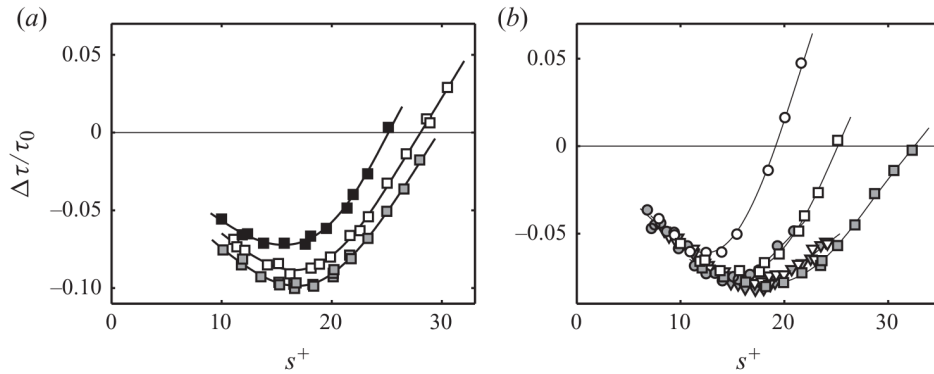
FIGURE 2. Drag reduction curves of various riblets, adapted from Bechert *et al.* (1997). (*a*) Blades with fixed height-to-spacing ratio, $h/s = 0.5$, and different tip width, t/s. Solid symbols, $t/s = 0.04$; open symbols, $t/s = 0.01$; grey, $t/s = 0.02$ with improved blade alignment and groove impermeability. (*b*) Riblets with approximately equal viscous slope m_s. ■, blades with $h/s = 0.4$ and $t/s = 0.01$; □, blades with $h/s = 0.5$ and $t/s = 0.04$; ●, scalloped groves with $h/s = 0.7$ and $t/s = 0.015$; ○, scalloped groves with $h/s = 1.0$ and $t/s = 0.018$; ▼, trapezoidal riblets with tip angle 30°; ▽, trapezoidal riblets, 45°.

Figure 2.5: Readaption of **DR** Curves from Berchert et al. (1997) by Jiménez (2011)

Investigation for different shapes of riblet cross-section and values of riblet spacing and height revealed that for every specimen, the drag reduction curve is follows a similar trend in terms of the relation between **DR** and s^+. This is observable in Fig. 2.5. in which the riblet of different cross sections have different s^+_{opt} and the critical value of s^+ where the reversal of drag reduction initiates but the overall curvature is similar.
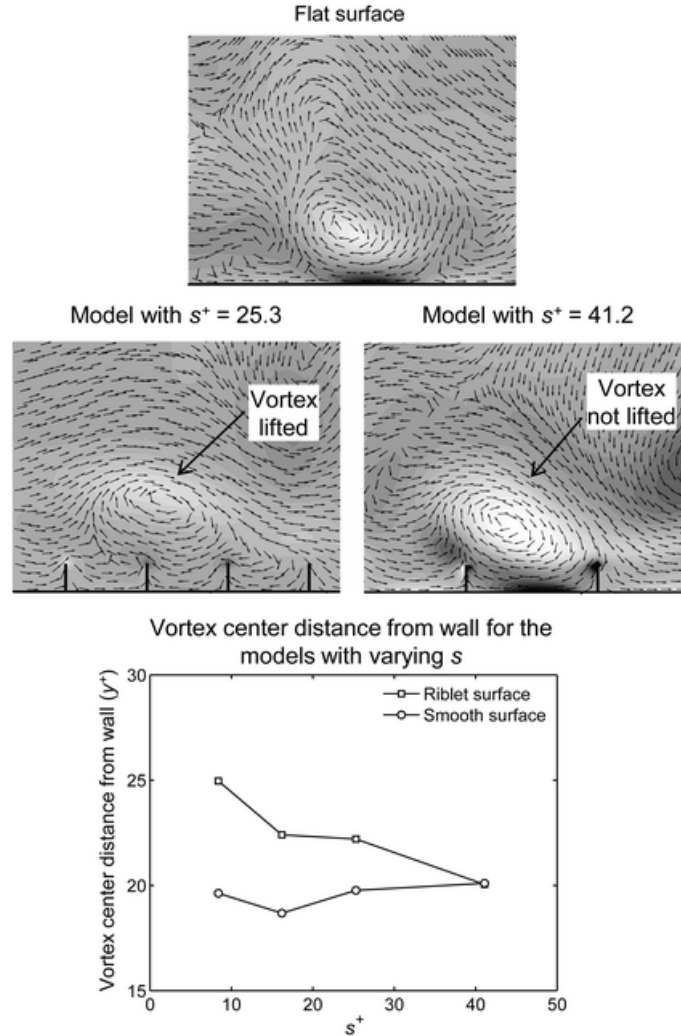
Figure 2.6: Depiction of how vortex center shifts downwards with increasing riblet spacing

This can be reasoned by the fact stated earlier that the dimension of the vortices induced above the riblet films are greater than the spacing between the riblets so, they stay afloat forming a stationary fluid film in the riblet spacings and the interaction only occurs with riblet tips. Fig. 2.6 shows how the vortex is not lifted in the case where it gets ample space between the riblets.

The normalized vertical distance y^+ of the vortex centers from the riblets walls decreases with progressively increasing rib spacing. As the vortex settles in these

spaces and the wetted area is increased(in comparison to the smooth plate) and the local flow in the vicinity of the riblet walls exhibits significantly higher gradients, the overall skin friction increases.

2.4   Applications in Aviation Industry

The efficiency benefits obtained from experimental and numerical investigations encouraged the implementation of these passive flow actuators to improve the energy efficiency in case of both internal flows (e.g. open and closed channel flows, pipe flows) and external flows(e.g. automobiles, marine vehicles, aircraft, gliders, etc.) With the emergence of global concerns about sustainable development, the deployment of these microstructures on sections of aircraft or aircraft as a whole becomes specifically useful in curbing emissions by reducing the amount of fuel being consumed.
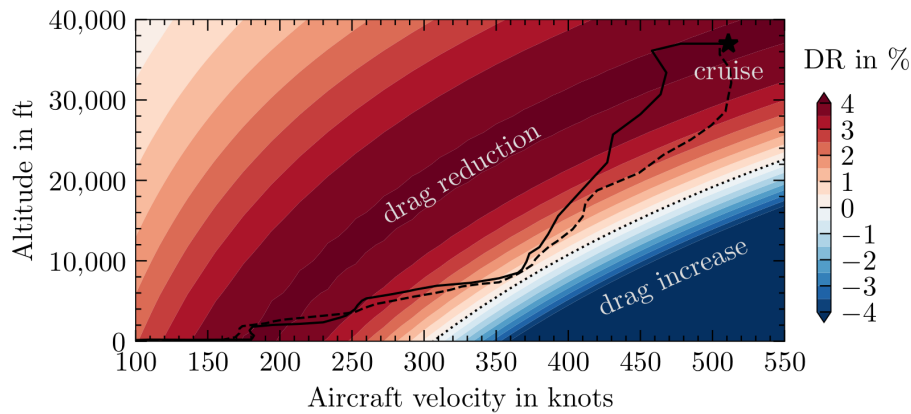
Figure 2.7: DR percentage incorporating riblet structures on aircraft. *Long haul flight from Melbourne to Los Angeles* **(Solid Line)**. *Short flight from Melbourne to Sydney* **(Dashed Line)**

The results from wind tunnel experiments have been validated by flight tests. Over 75% of its wetted area, an A320 research aircraft was covered in riblets. Fuel usage was assessed both with and without riblets. A 1.6% reduction in the aircraft's overall drag was noted under cruise circumstances. This outcome is in line with laboratory findings on the reduction of friction drag as well as the fact that only 75% of the aircraft's surface was covered with riblets and friction drag makes up roughly 45% of the total drag. In any event, an airplane would benefit greatly from such a reduction in drag.

A configuration of a typical regional aircraft with fully turbulent flow and natural laminar flow was studied using riblets deploying riblets only on the wing, only on the body, and combined wing and body (Catalano and Rosa).

In the findings, while riblets just on the body only produce an increase in drag that is fairly consistent with, riblets only on the wing are more effective at low incidences. When riblets are placed across the entire structure, a composite effect is achieved.

(a) C_f distribution on upper surface. Upper plot: Riblets-off; Lower plot: Riblets-on

(b) C_f at spanwise station $2y/b = 0.40$
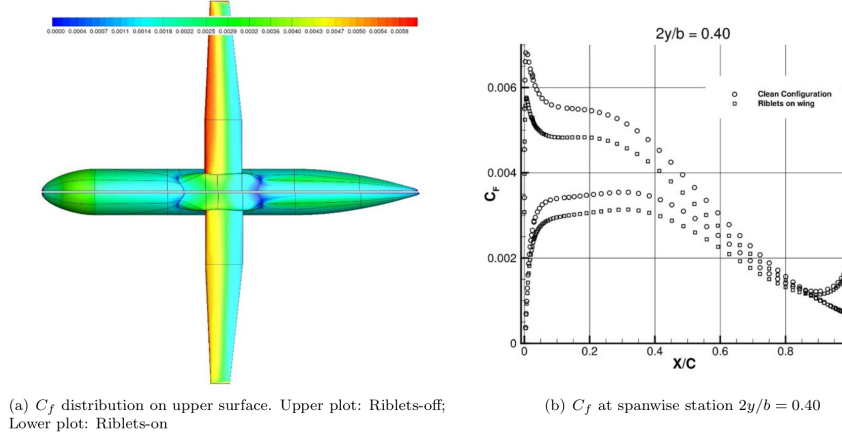
Figure 2.8: Drag Reduction with riblet on wings only.

(a) C_f distribution on upper surface. Upper plot: Riblets-off; Lower plot: Riblets-on

(b) C_f at a costant-y section of the body
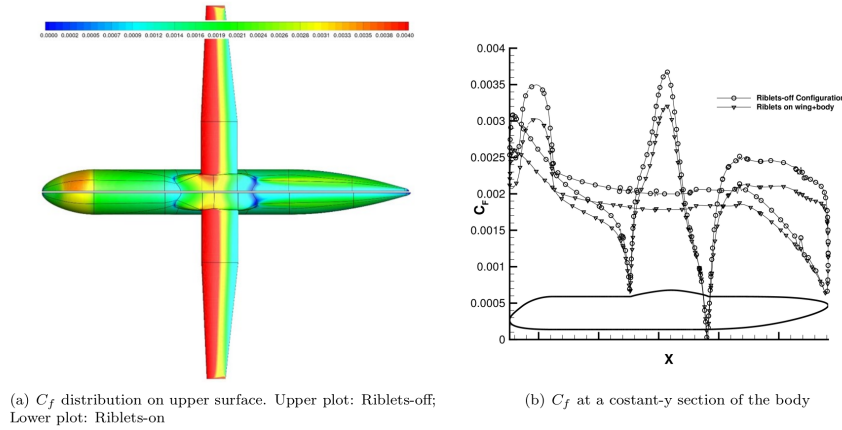
Figure 2.9: Drag Reduction with riblet on the body.

Quantitatively, the maximum total drag *(pressure drag + skin friction)*, ΔC_D reduction evaluated was about 9% which decreases with lift coefficient. While in terms of the skin friction alone, the maximum reduction, ΔC_f, was 11%.

The two figures show the comparison between the effect of installing riblets to wings only and the body on the reduction of surface skin friction against the configuration without riblets.

With the riblets installed only on the wings, it is clear that the forward portion of the wing experiences a noticeable reduction in skin friction. And with riblets on the body, the nose and the intersection of the wings and fuselage are the parts of the body where the riblets are most useful.

2.5   Convergent-Divergent Riblets

The longitudinal configurations of Riblets have been widely studied and analyzed for their effect on drag reduction properties. However, in recent decades, the emphasis has been laid on a more unconventional riblet geometry in which the directional arrangement of riblets forms two respective sections - Convergent and Divergent, as the name suggests. Convergent-Divergent riblets (also called Herringbone Riblets) are a sort of bio-inspired surface design, that has increased due to its potential to reduce skin friction and control flow separation.
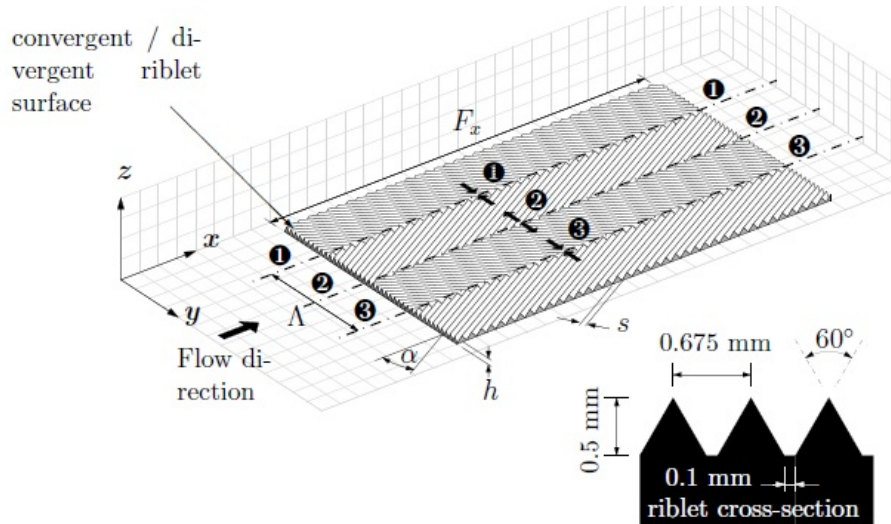
Figure 2.10: Schematic of the experimental setup for Flow Simulation over Convergent Divergent Riblets

As seen in **Fig. 2.7**, a general schematic of the configuration of a Converging-Diverging riblets section has been represented in which Λ represents the length of one wavelength of the riblets section consisting of one half of the Converging section and the other half of the Diverging section.

The Converging and Diverging Lines are defined with respect to the alignment of directional riblets with respect to the oncoming stream-wise flow, wherein if looked upon from the above, if the two sections seem to converge in the direction of flow, they lie on the Convergent Line and if they seem to diverge, they lie on the Divergent Line.

The angle γ represents the inclination of the axis of riblets with respect to the stream-wise flow direction. Essentially, $\gamma = 0$ would represent a longitudinal riblet

configuration. The length of riblet height above the smooth surface is denoted by h and the spacing between the adjacent edges of the intersection or riblet cross-section and the smooth surface by s.
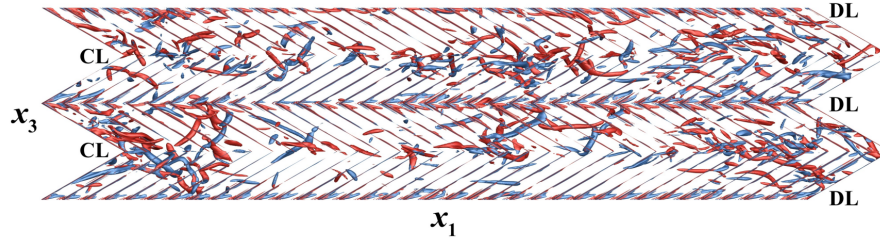
Figure 2.11: Direct Numerical Simulation of flow over a wavelength of Convergent-Divergent Riblets.

The intensity of swirling motion induced by the presence of the two directional sections leads to the generation of streamwise vortices which energize the boundary layer, resulting in a delay of flow separation.

Also, these vortices break up the eddies that would rather form in the state of transitional flow, preventing turbulence generation to some extent. The reduction of temporal perturbations of pressure in mean flow also leads to a reduction of noise generated due to the aeroacoustic phenomenon. Thus, Converging-Diverging riblet also reduces the overall noise generation in turbulent flows.

3
Theory

In this chapter, we discuss in brief the basic theory of fluid dynamics along with the computation of fluid flow involved. The governing equations of fluid flow are described and Also, the general characteristics of external flow over an immersed body is discussed.

3.1   External Incompressible Flow

Essentially, the flow over the flat plate with riblets is assumed to be incompressible since the velocity is quite lower than the threshold value of *Mach Number* range in which the compressibility effects of fluid flow are concerned. In the case of gases, compressibility effects are observed only after the Mach Number rises above 0.3. The motion of fluid for an external flow is unbounded and the study of external flow is an integral part of a number of subjects like aerodynamics, the study of heat and mass transfer, supersonic and hypersonic flows, etc.

The concept of Boundary Layer Flow introduced by Ludwig Prandtl witnessed the arrival of the theoretical establishment of modern fluid dynamics. It explained a lot of complex physical phenomena related to external viscous flow which had to be dealt with empirical relations developed by experimental results since the inviscid formulation by Euler failed to deal with these.
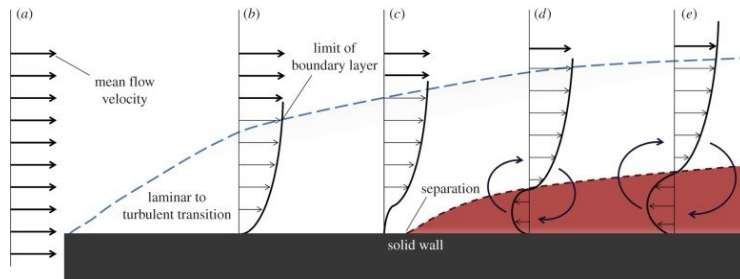
Figure 3.1: Boundary Layer Flow over a Flat Plate

A very primitive shape over which the development of boundary layers can be studied theoretically and numerically is a flat plate and the results obtained can be used to decipher the flow characteristics similar to various other bodies.

Using Thin Shear Layer (TSL) approximations, the analytical solution for the boundary layer can be derived using continuity and integral momentum equations. The assumptions in the local (s,n) coordinate system are :

$$v \ll u \tag{3.1}$$

$$\frac{\partial u}{\partial s} \ll \frac{\partial u}{\partial n} \tag{3.2}$$

$$\frac{\partial p}{\partial n} \approx 0 \tag{3.3}$$

where, n is the wall-normal axis and s lies along the wall surface.

The physical interpretation of these assumptions is that the velocity in the wall-normal direction is significantly lower than the shear flow, and the gradient of velocity along the surface is way less than the velocity gradient present in the wall-normal direction. The pressure gradient in the wall-normal direction can be neglected
The analytical solutions obtained for the boundary layer flow over a flat plate were found to be accurate with experimental and numerical investigations.

3.2 Governing Equations

The governing equations of fluid flow are the fundamental equations describing the physical laws on which the dynamics of fluid are based on. The three fundamental Conservation Principles are : (1.)*Conservation of Mass*, (2.)*Conservation of Momentum*, and (3.)*Conservation of Energy*.

$$\frac{\partial \rho}{\partial t} + \frac{\partial \rho u_i}{\partial x_i} = 0 \tag{3.4}$$

$$\frac{\partial \rho u_i}{\partial t} + \frac{\partial \rho u_j u_i}{\partial x_j} = -\frac{\partial p}{\partial x_i} + \frac{\partial \tau_{ij}}{\partial x_j} + \rho f_i \tag{3.5}$$

$$\frac{\partial \rho E}{\partial t} + \frac{\partial \rho u_j E}{\partial x_j} = -\frac{\partial p u_j}{\partial x_j} + \frac{\partial u_i \tau_{ji}}{\partial x_j} + \frac{\partial}{\partial x_j}\left(k\frac{\partial T}{\partial x_j}\right) + S_E \tag{3.6}$$

where, in the tensor form, i,j,k denote the three independent directions, f_i is the external body force, and S_E is the energy source. The fluid is considered to be Newtonian and the relation between stress tensor and viscosity is represented as τ_{ij} = $\mu(\partial u_i/\partial x_j + \partial u_j/\partial x_i) - \frac{2}{3}\mu\partial u_k/\partial x_k$.
In the set of partial differential equations, the unknown thermodynamic variables are : $\rho, p, i, and T$ Equations of state relate the other variables to the two state variables. Using ρ and T as state variables, we have state equations for p and i :

$$p = p(\rho, T) \quad and \quad i = i(\rho, T) \tag{3.7}$$

3.3   Finite Volume Method

The set of partial differential equations is converted into a set of linear algebraic equations by the finite volume approach. However, the discretization process utilized in the finite volume technique is unique and consists of just two simple phases. The partial differential equations are integrated and converted into balance equations over an element in the first stage. This entails employing an integrated quadrature of a specific order of precision to convert the surface and volume integrals into discrete algebraic relations over elements and their surfaces. A collection of semi-discretized equations is the end product. The second phase involves selecting interpolation profiles to approximate the variation of the variables inside the element, connecting the surface values of the variables to their cell values, and converting the algebraic relations into algebraic equations.

Invoking Gauss' Theorem for volume integrals is the essential first step before discretization of surface integrals.

Gauss's theorem, expressed using the divergence theorem in tensor notation, relates the volume integral of a vector field ϕ over a region CV to the surface integral of the vector field's flux ϕ through the closed surface S enclosing the region:

$$\int_{CV} \frac{\partial \phi_i}{\partial x_i}\, dV = \oint_S \phi_i n_i\, dS \tag{3.8}$$

where:

- $\int_C V$ represents the volume integral over Control Volume region CV,
- $\oint_S$ represents the surface integral over the closed surface ∂V,
- $\frac{\partial \phi_i}{\partial x_i}$ is the divergence of vector field ϕ,
- dV represents an infinitesimal volume element,
- n_i is the outward unit normal vector to the surface S, and
- dS represents an infinitesimal outward-pointing surface area element on the closed surface S.

The flow is laminar and steady and thus the discretization of temporal terms is not considered. We discuss the discretization of advective terms and diffusion terms in next sub-sections.

3.3.1   Discretization of Convective Term

The convective term in the Navier-Stokes equations accounts for the transport of momentum due to the bulk motion of the fluid. Before a suitable method of the discretization of the advection term can be deployed, it is converted to a simpler form using the Gauss Theorem :

$$\int_{CV} \frac{\partial \rho u_j \phi_i}{\partial x_j}\, dV = \sum_k \oint_{S_k} n_j \rho u_j \phi_i\, dS_k \tag{3.9}$$

where the integer k denotes the number of faces of the control volume.

We have used the bounded Upwind Scheme for the discretization of the Convective term. The linear upwind scheme is a discretization method commonly used in computational fluid dynamics to solve advection-dominated problems.

Consider a scalar quantity ϕ that is being advected by the velocity field in which the advection term is modeled as $\frac{\partial \rho u_i \phi}{\partial x_i}$.

The linear upwind scheme approximates the gradient of ϕ using a one-sided difference based on the direction of the velocity field:

$$\frac{\partial \phi}{\partial x} \approx \begin{cases} \frac{\phi_{i+1,j,k} - \phi_{i,j,k}}{\Delta x} & \text{if } U_{i,j,k} > 0 \\ \frac{\phi_{i,j,k} - \phi_{i-1,j,k}}{\Delta x} & \text{if } U_{i,j,k} \leq 0 \end{cases} \tag{3.10}$$

where:

- $\phi_{i,j,k}$ represents the value of ϕ at grid point (i, j, k),
- $U_{i,j,k}$ is the x-component of the velocity at grid point (i, j, k),
- Δx is the grid spacing in the x-direction.

This scheme ensures that the numerical solution uses information from the upstream direction of the velocity field, reducing numerical diffusion for advection-dominated problems.

Bounding the linear upwind scheme involves incorporating the velocity gradient to prevent excessive numerical oscillations. This can be achieved by limiting the gradient used in the linear upwind discretization. In index notation (i, j, k), the mathematical formulation of the bounded linear upwind scheme can be expressed as follows:

To bound this scheme using the velocity gradient, we can modify the gradients as follows:

$$\frac{\partial (\mathbf{U}\phi)}{\partial x} \approx \begin{cases} \min\left(\frac{\phi_{i+1,j,k} - \phi_{i,j,k}}{\Delta x}, \max(0, \nabla U_{i,j,k})\right) & \text{if } U_{i,j,k} > 0 \\ \min\left(\frac{\phi_{i,j,k} - \phi_{i-1,j,k}}{\Delta x}, \max(0, -\nabla U_{i,j,k})\right) & \text{if } U_{i,j,k} \leq 0 \end{cases} \tag{3.11}$$

where $\nabla U_{i,j,k}$ represents the gradient of the x-component of the velocity at the grid point (i, j, k). The min function ensures that the bounded gradient is always smaller than or equal to the original linear upwind gradient, and the max function prevents the gradient from becoming negative in the opposite direction of the velocity.

By incorporating the velocity gradient in the bounded linear upwind scheme, numerical oscillations can be mitigated while still capturing the advection characteristics of the flow.

By incorporating the velocity gradient in the bounded linear upwind scheme, numerical oscillations can be mitigated while still capturing the advection characteristics of the flow.

3.3.2 Discretization of Diffusion Term

The diffusion term in the Navier-Stokes equations (which is of the form : $\frac{\partial}{\partial x_i}\left(\Gamma\frac{\partial u_i}{\partial x_i}\right)$) represents the effects of molecular viscosity in fluid flow. It describes how momentum is transferred between adjacent fluid particles due to their relative motion and interaction on a microscopic scale. The integration over control volume and conversion into surface integrals take the form :

$$\int_{CV} \frac{\partial}{\partial x_i}\left(\Gamma\frac{\partial}{\partial x_k}\phi\right) dV = \sum_k \oint_{S_k} n_j \Gamma u_j \frac{\partial \phi}{\partial x_j}\, dS_k \tag{3.12}$$

Calculating gradients at the surface of the control volumes will be needed for this. The gradients of the cell centers can be calculated, and the value on the cell faces can then be determined using interpolation. The average value across the cell is essentially used for estimating the gradient's value at the cell center P:

$$\left(\frac{\partial \phi}{\partial x_i}\right)_P \approx \frac{\int_\Omega \frac{\partial \phi}{\partial x_i}\, d\Omega}{\Delta\Omega} \tag{3.13}$$

This is further simplified using the Finite Volume Method approximation and can be written as:

$$\left(\frac{\partial \phi}{\partial x_i}\right)_P \approx \frac{\sum_k \phi_k \Delta S_k n_i^{(k)}}{\Delta\Omega} \tag{3.14}$$

where $n_i^{(k)}$ is the outward normal of the surface k in the control volume. After being calculated, the gradients can then be interpolated to the faces. After being calculated, the gradients can then be interpolated to the faces.

3.3.3 SIMPLE Algorithm and simpleFoam

SimpleFoam is a steady-state solver for incompressible, turbulent flow, using the SIMPLE (Semi-Implicit Method for Pressure Linked Equations) algorithm.

The solver is an incompressible steady-state solver. Since there is no connection between the momentum and continuity equations due to the incompressibility, it is not necessary to solve the energy equation. Instead, the momentum equation is resolved, and a pressure adjustment is carried out, leading to the discovery of pressure differences rather than the solution of physical pressure.

The SIMPLE algorithm (Semi-Implicit Method for Pressure-Linked Equations) is a numerical technique used for solving incompressible Navier-Stokes equations. It efficiently couples the velocity and pressure fields to ensure mass conservation and accurate simulation of fluid flows.
Since there is no connection between the momentum and continuity equations due to the incompressibility, it is not necessary to solve the energy equation. Instead, the

momentum equation is resolved, and a pressure adjustment is carried out, leading to the discovery of pressure differences rather than the solution of a physical pressure. A Poisson equation for the pressure is discovered if the divergence of the momentum equation is taken, and the term $\frac{\partial}{\partial x_k}\left(\frac{\partial}{\partial t}\rho u_k\right)$ is expanded using the continuity equation :

$$\frac{\partial}{\partial x_i}\left(\frac{\partial p}{\partial x_i}\right) = -\frac{\partial}{\partial x_i}\left[\frac{\partial}{\partial x_j}(\rho u_i u_j - \tau_{ij})\right] + \frac{\partial(\rho g_i)}{\partial x_i} + \frac{\partial^2 \rho}{\partial t^2} \tag{3.15}$$

The SIMPLE algorithm solves the momentum equation and the above Poisson pressure equation. The solver `simpleFoam` follows these steps iteratively:

1. Solve the momentum equations for the intermediate velocity field u_i^*:

$$\rho\frac{\partial u_i^*}{\partial t} + \rho u_j\frac{\partial u_i^*}{\partial x_j} = -\frac{\partial p}{\partial x_i} + \mu\frac{\partial^2 u_i^*}{\partial x_j \partial x_j}$$

2. Solve the pressure correction equation to obtain the pressure correction field ϕ:

$$\frac{\partial^2 \phi}{\partial x_i \partial x_i} = \frac{\partial u_i^*}{\partial x_i}$$

3. Update the velocity field U_i using the pressure correction:

$$u_i^{n+1} = u_i^* - \frac{\partial \phi}{\partial x_i}$$

4. Update the pressure field using the pressure correction:

$$p^{n+1} = p^n + \phi$$

4

Methodology

This chapter outlines the methodology deployed to investigate the effects of microstructural riblet grooves on laminar boundary layer flow. The research seeks to comprehend how these riblet grooves influence flow characteristics and their potential to control drag reduction. The procedures undertaken in the complete setup are described. SolidWorks and Salome were used for geometry creation and/or modification, while the meshing was handled using Salome. The case was using OpenFoam solver, simpleFoam, which is essentially an incompressible solver deploying the SIMPLE (Semi-Implicit Method for Pressure-Linked Equations) algorithm.

4.1   Case Setup

The setup for the validation case essentially comprised of incorporating the geometry of a Convergent-Divergent riblet section on a smooth flat plate. The riblets are installed at a certain distance from the leading edge of the flat plate so that the boundary layer develops before reaching it The section of riblets along with the rest of the smooth sections of the plat plate act as the walls.
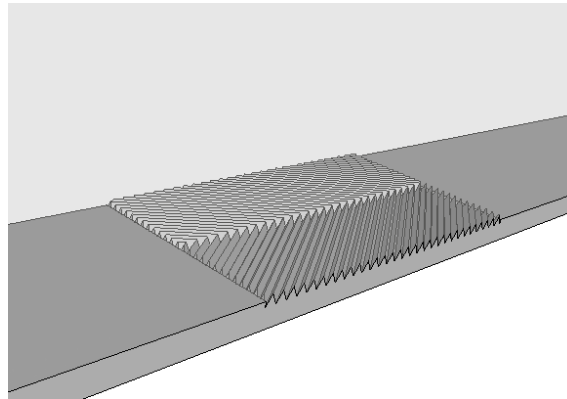
Figure 4.1: Geometry of Riblet section installed on flat plate

The Convergent-Divergent sections are called so because of the configuration of the arrangement of riblet patterns across the length of streamwise flow direction. If the +ve x - direction is considered as the streamwise direction, then looking from the top, the riblet patterns seem to converge over a line. Two sections of riblet patterns combined consist of a single wavelength of riblet sections. Such a riblet

wavelength when extended in either direction produces a riblet section with multiple wavelengths.

4.1.1 Geometry

For the validation case, we chose the geometry with reference to Xu et al.(2018) and Tongbiao(2020) keeping in mind that this geometry configuration is kept constant with the rest of the simulation which involved a yawed riblet section. As shown in **Fig. 4.2**, the origin is located at the center of riblet wavelength Λ, with the x - direction aligned towards the streamwise flow direction, the y - direction towards the wall-normal direction and the y - direction.
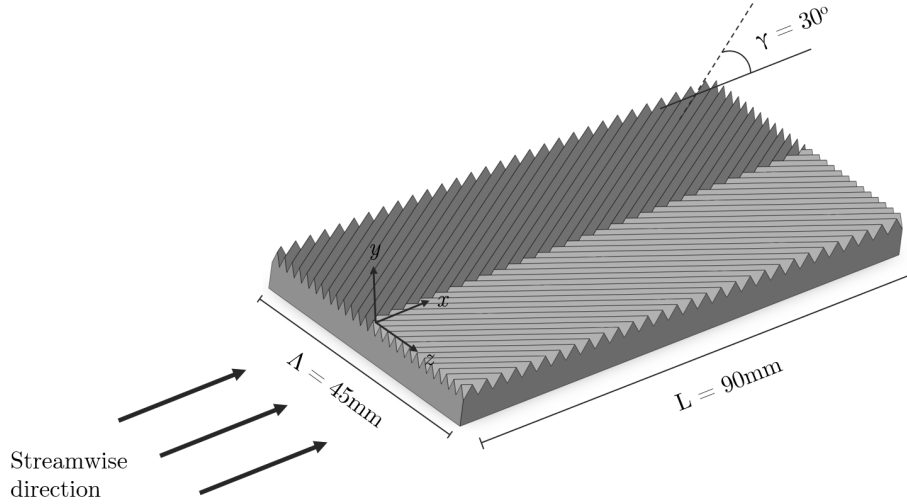
Figure 4.2: Geometrical parameters of Validation Case

Later, the origin was shifted the distance of half a wavelength in the z - direction for the sake of comparison and analysis of results but that doesn't affect the overall results since the symmetricity of flow in the span-wise direction takes care of it.

The geometrical parameters for the specific riblet configuration are :

     - Riblet Section Wavelength ($\boldsymbol{\Lambda}$) : 45 mm
     - Length of riblet section in streamwise direction (L) : 90 mm
     - Angle of Yaw (γ) : 30°

where the angle of yaw (γ) is the angle that the riblet passage makes with the streamwise direction.

4.1.2 Computational Domain

The actual computational domain consists of six patches in total with the wall patch being derived from the surface of the flat plate. The domain is extended upwards to imitate the inflow of fluid from the far stream and the portion of flat pate below the wall surface is eliminated.
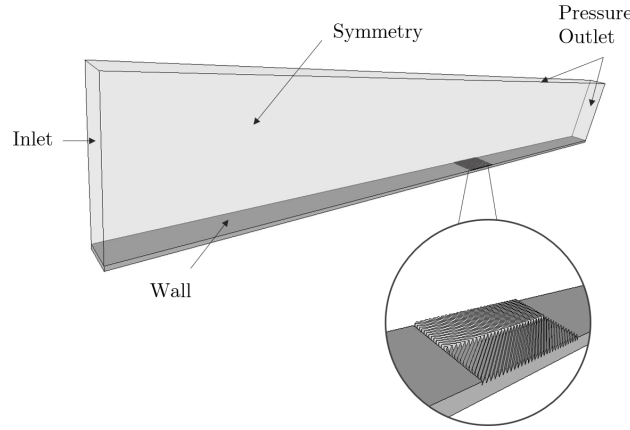
Figure 4.3: Illustration of the Computation Domain for the generic case

The parameters associated with the computational domain are :

- Total plate length : 1380 mm
- Riblet Section length : 90 mm
- Plate and Riblet width : 45 mm
- Distance of Riblet section from leading-edge : 670 mm
- Local Boundary layer length $(\delta_{\mathbf{s}})_{\mathbf{x=0}}$: 12.7 mm
- Domain height : $\mathbf{15\delta_s}$
- Reynolds Number at the trailing edge of Plate ($\mathbf{Re_L}$) : 1.375×10^5

4.1.3 Computational Grid

The computational grid was generated using Salome meshing module and exported in `.unv` format, easily workable in openFoam. The mesh file is imported in open-Foam environment using the command `"ideasUnvToFoam"`.

The $\mathbf{Netgen1D - 2D - 3D}$ algorithm was used to generate the grid using tetrahedral volumes. Adding prism layers was a daunting task and the mesh morphing to external layers with the prism layer cells was not made possible. To compensate, the grid size was significantly reduced near the wall regions and let to gradually grow towards the far stream. (**Fig**.**4.4**)

23

For the sake of the grid independence study (discussed in later chapter), 6 mesh configurations were created. The overall pattern of mesh resolution was kept constant keeping in mind the refinement zones.(**Fig**.**4.5**)
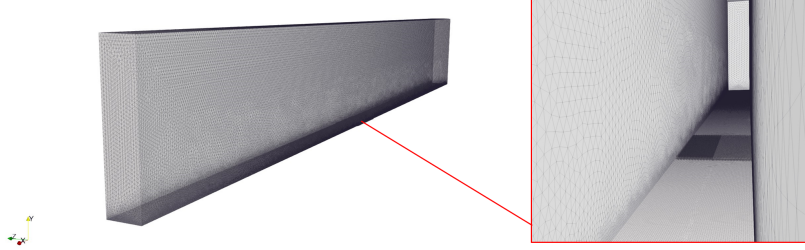
Figure 4.4: Grid configuration for the case

The values of flow fields obtained from a fixed probe location saturated between the 5th and 6th grid configuration (**Table 4.1**). However, the 6th grid was chosen because of better mesh quality.
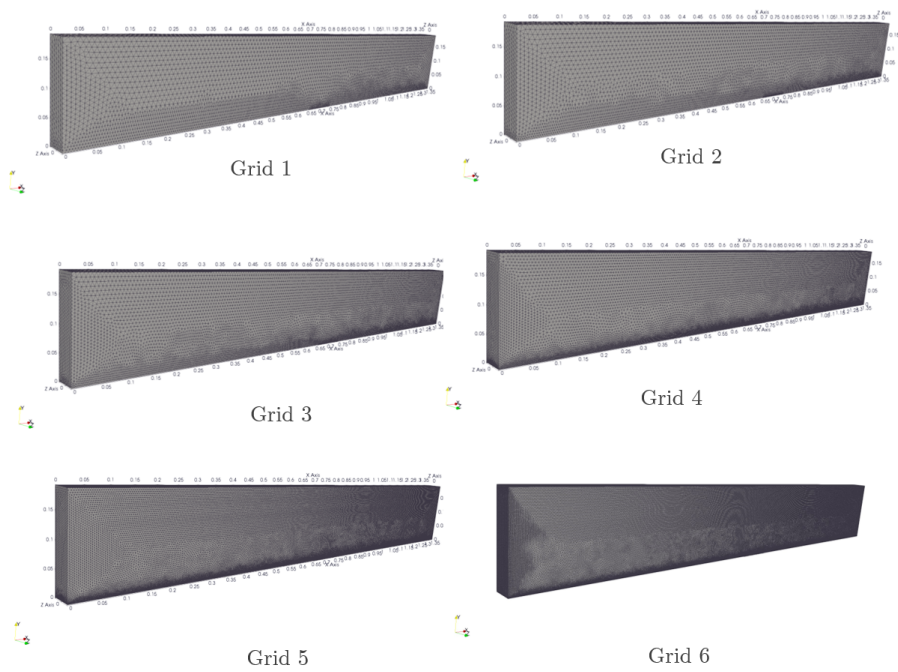
Figure 4.5: Grid sizes considered for mesh independence study

The table provides the values of velocity probes at a fixed location that were obtained for different sizes of grid resolution. The validation plots as discussed in a

later chapter were matched against every consecutive grid resolution and the best accuracy was obtained with Grid 6. Thus, it was finalised for the rest of the cases.

Table 4.1: Grid Resolution vs. Probe Location Value (u_x; m/s)

Grid No.	Grid 1	Grid 2	Grid 3	Grid 4	Grid 5	Grid 6
Resolution	2×10^5	2.5×10^5	5×10^5	1.5×10^6	5.4×10^6	1.05×10^7
Probe Value	0.100606	0.100638	0.100762	0.10077	0.100728	0.100713

The quality metrics for the imported mesh were generated using the `"checkMesh"` functionality :

```
$ checkMesh -allGeometry -allTopology -writeAllFields -writeSets vtk
```
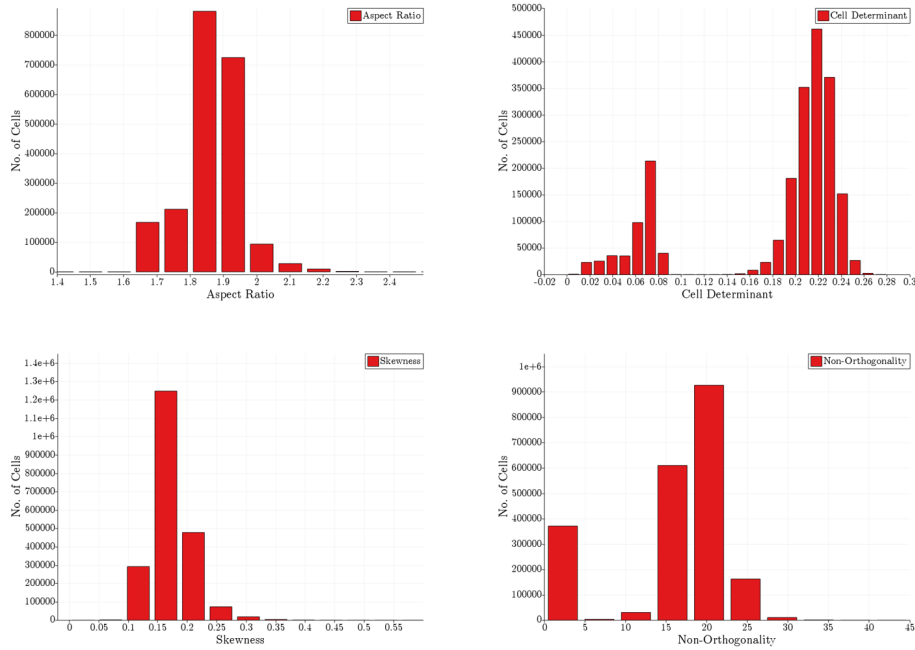

Figure 4.6: Mesh Quality Metrics. Clockwise from top left : *(a.) Aspect Ratio, (b.) Cell Determinant, (c.) Non-orthogonality* , and *(d.) Skewness*

The mesh quality metrics are important to investigate before moving on with running the solver because the nature of the solution schemes and the accuracy, stability, and convergence involved heavily depend on the mesh quality.

The values of the mesh quality metrics lay well within the acceptable range and thus the given mesh configuration was alright to work with. In all the future grids, similarly quality checks were carried out.

4.2   OpenFoam Setup

Once grid generation was done and imported into openFoam environment and the necessary checks done, the directory was set up for running the simulation.

The `0` folder was created containing the boundary conditions for pressure, `p` and velocity, `U` fields.

The entries in the `U` dictionary are given below :

```
FoamFile
{
    version     2.0;
    format      ascii;
    class       volScalarField;
    object      U;
}
// * * * * * * * * * * * * * * * * * * * * * * * //

dimensions      [0 1 -1 0 0 0 0];

internalField   uniform (0.1 0 0);

boundaryField
{
    inlet
    {
        type            fixedValue;
        value           $internalField;
    }
    outlet
    {
        type            zeroGradient;
    }
    top
    {
        type            zeroGradient;
    }
    wall
    {
        type            fixedValue;
        value           uniform (0 0 0);
    }
    frontSymmetry
    {
        type            symmetryPlane;
```

```
    }
    backSymmetry
    {
        type            symmetryPlane;
    }

}



// ********************************************* //



Similarly, the entries in p dictionary specified are given below :



FoamFile
{
    version     2.0;
    format      ascii;
    class       volScalarField;
    object      p;
}
// * * * * * * * * * * * * * * * * * * * * * * * //

dimensions      [0 2 -2 0 0 0 0];

internalField   uniform 0;

boundaryField
{
    inlet
    {
        type            zeroGradient;
    }
    outlet
    {
        type            fixedValue;
        value           uniform 0;
    }
    top
    {
        type            fixedValue;
        value           uniform 0;
    }
    wall
    {
```

```
        type            zeroGradient;
    }
    frontSymmetry
    {
        type            symmetryPlane;
    }
    backSymmetry
    {
        type            symmetryPlane;
    }
}



// ********************************************* //
```

In the `transportProperties` dictionary, the `transportModel` was chosen as Newtonian, and the kinematic viscosity value was given of that of water :

```
FoamFile
{
    version     2.0;
    format      ascii;
    class       dictionary;
    object      transportProperties;
}
// * * * * * * * * * * * * * * * * * * * * * * * //

transportModel  Newtonian;

nu              0.0000010034;

// ********************************************* //
```

Since the flow is steady, laminar modeling of flow was specified in `turbulenceProperties` dictionary :

```
FoamFile
{
    version     2.0;
    format      ascii;
    class       dictionary;
    object      turbulenceProperties;
}
```

```
// * * * * * * * * * * * * * * * * * * * * * * * //

simulationType    laminar;

// ********************************************* //
```

The `controlDict` file shown below mentions the initial conditions and the total simulation time specified. Since the simulation is the total time steps can be thought of as the total iterations for the convergence of solution (discussed in later chapter).

```
FoamFile
{
    version     2.0;
    format      ascii;
    class       dictionary;
    object      controlDict;
}
// * * * * * * * * * * * * * * * * * * * * * * * //

application    simpleFoam;
startFrom      latestTime;
startTime      0;
stopAt         endTime;
endTime        50;
deltaT         0.01;
writeControl   timeStep;
writeInterval  1;
purgeWrite     1;
writeFormat    ascii;
writePrecision 8;
writeCompression off;
timeFormat     general;
timePrecision  8;
runTimeModifiable true;

// ********************************************* //
```

For additional post-processing purposes, functions including `residual` and `wallShearStress` have been included in the `controlDict` file for further analysis :

```
functions
{
    wallShearStress
```

```
            {
#include "wallShearStress"
            }

    residuals
            {
                #include "residuals"
            }
}
```

For all the other cases with different Reynolds Numbers and different yaw configurations, the mesh resolution openFoam case structures were kept the same except for the inlet velocity for different Reynolds Numbers and yaw angles for the other two yaw configurations. The mesh metrics were investigated at every instance and non-orthogonal corrections were deployed in some cases which required so.

5

Results and Discussion

The results obtained for different values of Reynolds Number and yaw angles are discussed in this chapter. First off, the results obtained from the first case with $\gamma = 30^o$ are validated against the data from experimental and computational results previously obtained through literature review. The dimensions of the flat plate and riblet sections were kept intact as in the experimental setup. The total length of the flat plate is 1.38 m, the riblet section length is 90 cm, the rib spacing of 3mm, and the riblet height is 2.4 mm. The wavelength of the riblet section was 45 mm and the percent protrusion of the riblets from the surface of the flat plate was kept 50%. That is to say that the total height of the riblet section above the surface of the flat plate was 1.2 mm. The y-direction was normalized using the thickness length of the boundary layer in the case of a smooth flat plate and the z-direction using the wavelength of the riblet. The distance of the riblet section from the leading edge of the flat plate was kept at 0.67 m to comply with the setup of the experimental investigation which was referred to for validation.

5.1   Convergence of Solution

Two convergence studies were carried out in order to investigate the accuracy of solution parameters and mesh sizing. First off, in order to realize the mesh size for an accurate description of the flow, a mesh independence study was carried out.
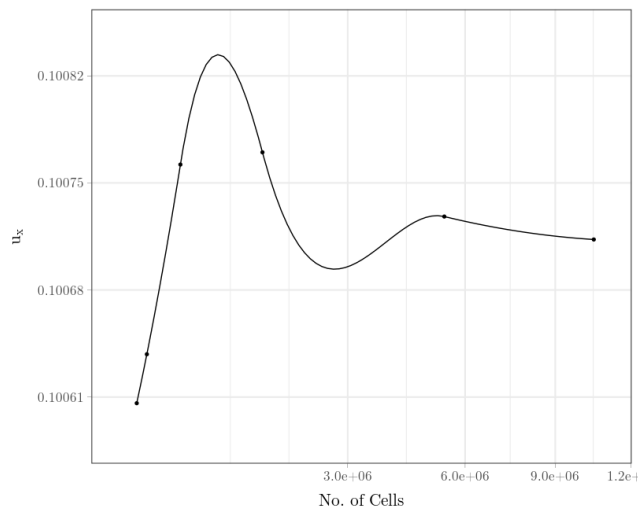

Figure 5.1: Mesh Independence Study

As can be seen from Figure 4.1, the variation of velocity in the x-direction was less than 0.015%, so the grid size parameters for the final mesh resolution were chosen for further computation which in the validation case was approximately 10.5 million volume cells.

The mesh convergence study provides a metric for the grid resolution that is apt for the current study and further reducing the size won't affect the solution. The second convergence study revolves around the solution in which the residuals are analyzed so as to ensure that the steady-state approach can be chosen for further studies and also to ensure the number of iterations is enough for the convergence of the solution.
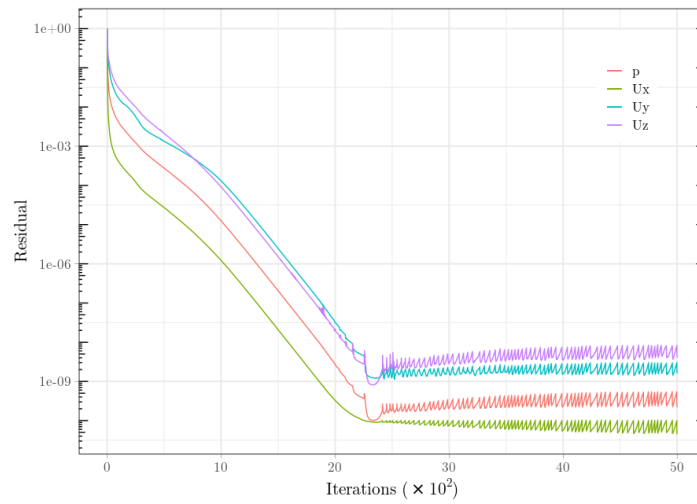

Figure 5.2: Residuals Plot

The residuals obtained from the simulation dropped well below 10^{-08} for all the flow variables, which can be assumed to be sufficient for the simulation to converge. The maximum fluctuations in the residual values are of the same order, so the flow can be considered inherently steady and laminar. For the rest of the simulation cases, the residuals behavior was investigated at every instance and found to be pretty similar.

5.2   Validation of Results

The results obtained for the case with a yaw angle of $\gamma = 30^o$ is validated against the experimental data from Xu et al.(2018) and Tongbiao et al.(2020). The results seem close enough considering the complexity of flow in the micro-structural grooves.

The first plot shows the dimensionless horizontal velocity in x direction, u^*, normalized by the freestream velocity ($u^* = u/U_\infty$) against the dimensionless wall-normal distance, y^*, normalized by the local boundary layer thickness δ_s ($y^* = y/\delta_s$) of that of a smooth plate (at a distance of 0.03 m before the start of riblet section).

The values are pretty much the same as that of the experimental results obtained from Xu et al.(2018), which in turn fit very well with the analytical Blasius solution curve signifying that the flow is yet not influenced by the riblet section and exhibits the same velocity as of a smooth flat plate.

The second and third plot shows the normalized velocity plot against the normalized wall normal distance at two extreme ends of the riblet wavelengths(Convergent Line and Divergent Line) at a distance of 0.045 m and 0.075 m from the initiation of the riblet section respectively.

As can be seen, the maximum deviation of the velocity profile from the experimental values is acceptable enough to proceed with the mesh resolution used. The CL and DL notations denote the convergent line and divergent line respectively.
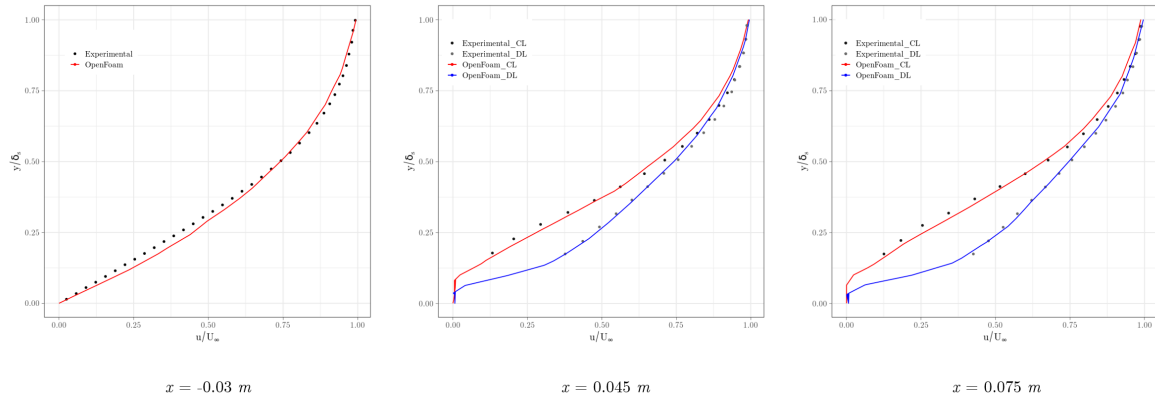

Figure 5.3: Longitudinal velocity profile curves at three instances.

It can be observed that the riblets alter the velocity profile from the Blasius curve at the convergent and divergent lines in the opposite manner. While the normalized velocity, u^* in the x-direction increases at the convergent line in the middle of the boundary layer ($y^* \approx 0.25 - 0.5$), it gets re-aligned to the Blasius curve as the wall-normal distance approaches the boundary layer thickness ($y^* \approx 1$).

Similarly, at the divergent line, the magnitude of u^* reduces a bit midway through the boundary layer ($y^* \approx 0.15 - 0.5$) before it, too, gets re-aligned to the Blasius curve at the tip of the boundary layer ($y^* \approx 1$).

5.3 Influence of Riblets on Flow Properties

Qualitatively, the velocity contours in the three normal directions at a distance of x = 0.045m from the origin of the riblet section is represented by **Fig. 4.4** depicting the overall redistribution of the velocity profiles influenced by the presence of the riblets.

It can be inferred from the longitudinal velocity plot that the effect of the riblets in the far-field region is not profound. However, close to the riblet sections, it can be seen that the longitudinal velocity in the grooves spacings is negligible ($u_x \approx 0$).

The velocity contours in the y direction exhibit varying behaviors up to the length of the boundary layer. At the edges of Divergent Lines ($z = \pm 0.0225m$), close to the riblet walls, the wall-normal velocity, u_y, becomes negative. Moving upwards, the velocity decreases in magnitude up to the length of the boundary layer and changes its sign just upwards of the boundary layer length.
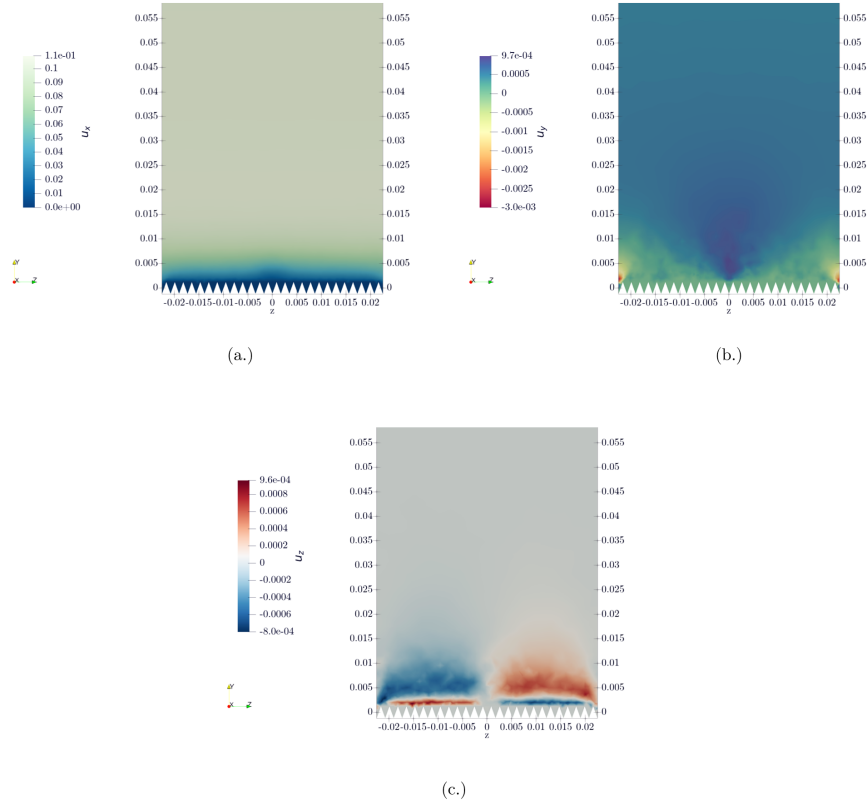

(a.)   (b.)

(c.)

Figure 5.4: Velocity component contours *(a) Longitudinal Velocity, (b) Wall-Normal Velocity,* and *(c) Spanwise Velocity* at $x = 0.045$m

While at the Convergent Line ($z = \pm 0m$), it can be seen that the wall-normal velocity is close to zero in the riblet spacing, and suddenly rises to a positive value, up to the length of the boundary layer thickness (δ_s) above which it becomes uniform over both Convergent Line and Divergent Lines.

Two halves with alternate velocity directions can be seen in the velocity contours for z direction. In the region between the Convergent Line ($z = 0$), and the left Divergent Line (z = -0.0225m), the z-velocity, u_w, is positive constituting a thin layer just above the riblets. It goes to zero and then becomes negative in the positive y direction. While in the region between the Convergent Line ($z = 0$), and the

right Divergent Line ($z = 0.0225$m), the opposite pattern exists with a thin layer of negative u_w which increases to zero and becomes positive with increasing y-distance.

Quantitatively, the normalized velocity profiles in all normal directions (i.e. $u^* = u/U_\infty$, $v^* = v/U_\infty$, $w^* = w/U_\infty$), against the normalized y-direction distance ($y^* = y/\delta_s$) has been visualized in (**Fig. 4.5**).

For the value of $y/\delta_s \approx 0.005 - 0.01$, the value of u/U_∞ at the Convergent Line is less than that of at the Divergent Line. This is reversed just after $y/\delta_s \approx 0.005 - 0.01$ and up until $y/\delta_s \approx 1$, it remains that way. The velocities at two lines converge at this point and for $y/\delta_s > 1$, the velocities over both Convergent Line and Divergent Line remain the same.
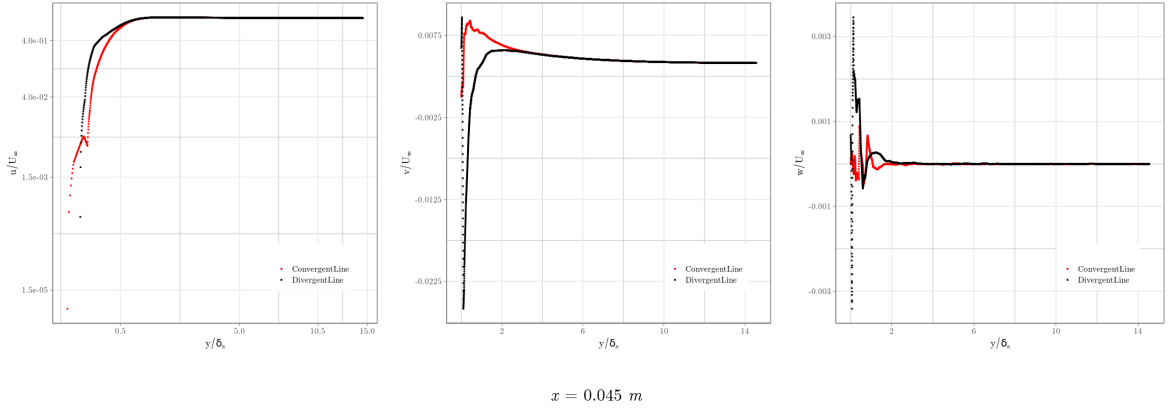

$x = 0.045\ m$

Figure 5.5: Normalized Velocity vs Normalized y - Distance *(a) Longitudinal Velocity, (b) Wall-Normal Velocity,* and *(c) Spanwise Velocity* at $x = 0.045$m

The values of normalized y-velocity, v/U_∞ are opposite near the riblet wall at Convergent Line and Divergent Line. However, in the riblet groove over the Divergent Line, for $v/U_\infty \approx 0$, it is in the same direction as that over the Convergent Line. It turns negative above the riblet as the y-distance increases. Over the Convergent Line, the velocity is nearly zero and increases to a maxima before decreasing.

In case of normalized z-velocity, the values oscillate about 0 initially up to the length of $y/\delta_s \approx 2$. The oscillations for the z-velocity over the Divergent Line are more amplified as compared to that over the Convergent Line.

5.3.1 Velocity Field and Streamlines

From what was observable in the previous section, the velocity contours and the nature of velocity distribution over the Convergent and Divergent Lines suggested a swrling flow in the cross-stream plane (*y-z* plane) over the section of riblets induced by them.
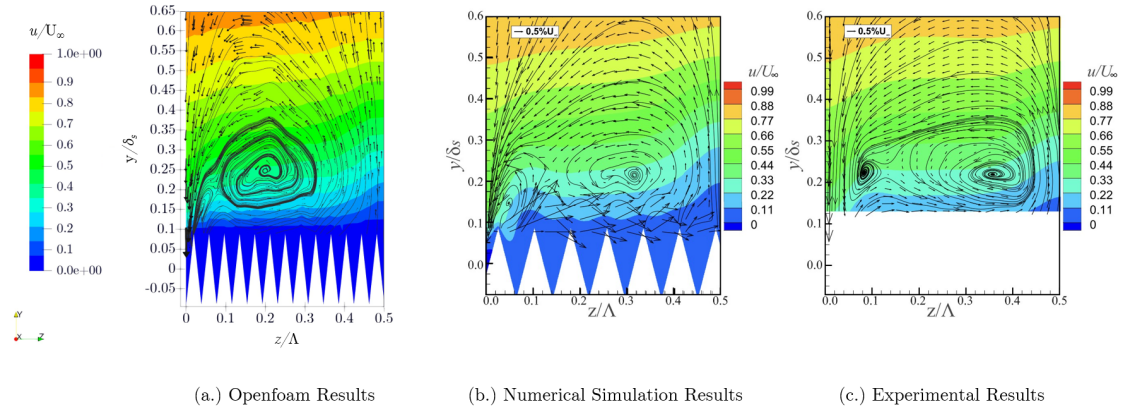
35

(a.) Openfoam Results   (b.) Numerical Simulation Results   (c.) Experimental Results

Figure 5.6: Velocity Streamlines and Glyphs Representation comparison at $x = 0.075$m for current results, Tongbiao(2020), and Xu et al.(2018)

The left-most representation depicts the essential characteristics of the flow that has been captured through the current simulation. It is close to what was obtained through the numerical simulation by Tongbiao(2020) and Xu et al.(2018). The down-wash and up-wash motion over the Divergent Line and the Convergent Line respectively indeed conform with the velocity distribution plot. As can be seen, there are two vortex zones present in the span-wise flow which is closely accurate with the reference plots.

5.3.2   Longitudinal Development of Vortices

The vortices induced by the riblets gradually develop with the thickness of the local boundary layer. As can be seen from **Fig. 4.7**, at a distance of $x = 0.015$m, the velocity streamlines are vertical over the Convergent Line but near the Divergent Line at the left edge, swirling motion can be observed.

This gets amplified with increasing distance from the Riblet Section as can be seen in the subsequent sections of y-z plane. The primary vortex grows in size and bifurcates into two at a distance of $x = 0.06$m. The center of the secondary vortex shifts towards the Convergent Line at $x = 0.075$m and grows in size. At $x = 0.08$m, it further bifurcates into two, giving rise to three vortex centers in total.

The overall motion of the fluid in the cross-stream direction seems to be generated from the Convergent Line with an up-wash motion and circulating across the half length of the riblet section towards the Divergent Line.

The flow is symmetrical about the Convergent Line and a similar pattern of flow is present in the other half of the riblet section wavelength.
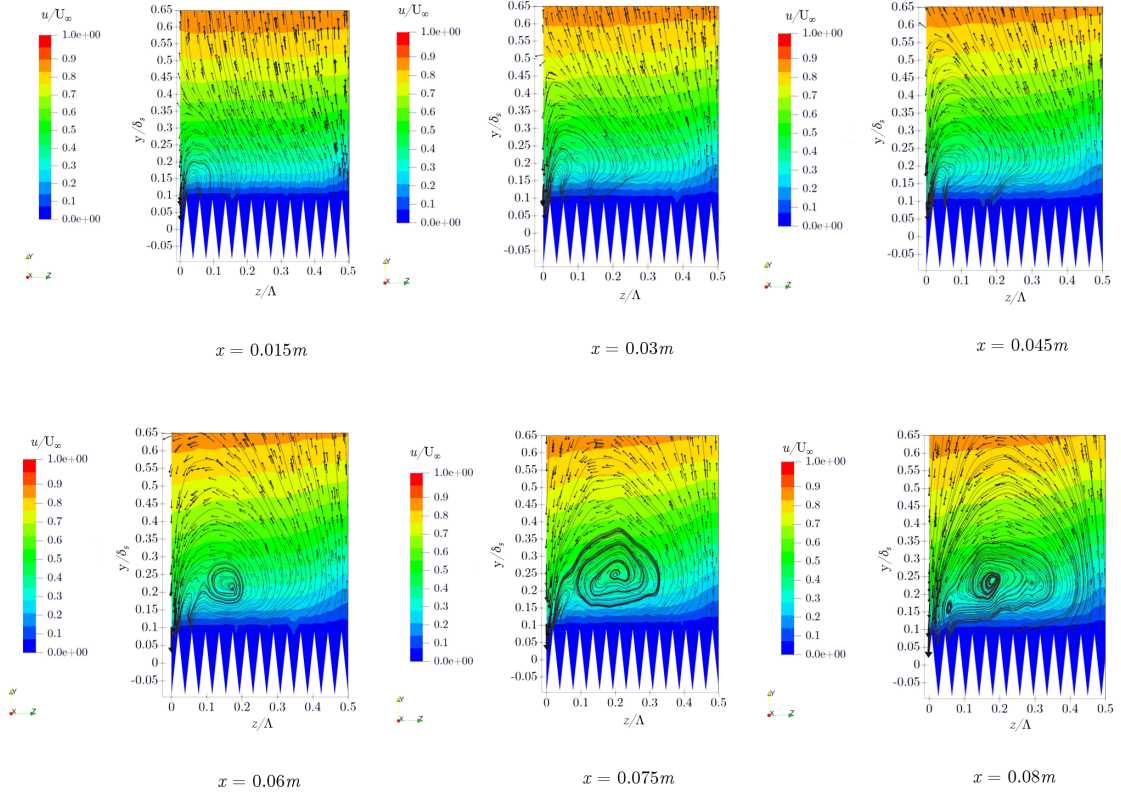
x = 0.015m   x = 0.03m   x = 0.045m

x = 0.06m   x = 0.075m   x = 0.08m

Figure 5.7: Representation of Vortex Development at different values of Longitudinal Distance from the origin of Riblets Section

5.3.3 Helicoidal Motion Inside Riblet Valleys

According to the experimental results by Xu et al.(2018) using dye visualization, it was deduced that the motion of the fluid in the riblet valleys differs from that of longitudinal riblets. The cross-stream velocity distribution interacts with the axial velocity of the riblets' fluid flow, giving rise to a helicoidal motion (**Fig. 4.8**).
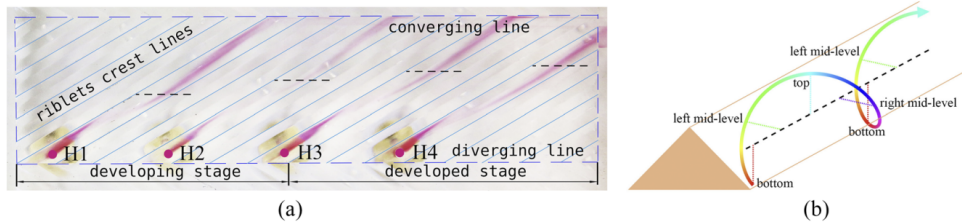

Figure 5.8: Dye visualization of flow in riblet spaces (Xu et al.(2018)). *(a) the dye is injected at orifices H1-H4*, and *(b) illustration of the helicoidal motion*

As stated, it is possible to think of the flow within the riblet valley as a channel flow influenced by a freestream crossflow with a yaw angle, γ.

The helicoidal motion in the riblet valleys, indeed, has been confirmed in our numerical simulation. As can be seen from **Fig. 4.9**, the motion at the crest of riblet valleys is nearly stationary with the glyphs aligned in the longitudinal direction.
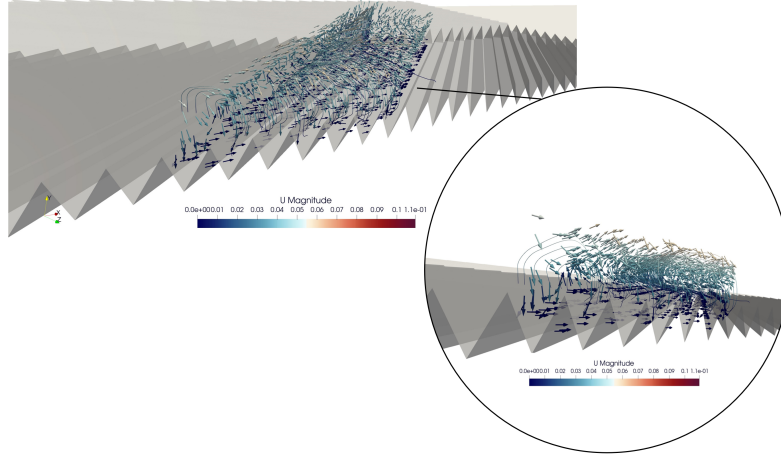

Figure 5.9: Helicoidal motion in riblet valleys. Top view and (*circle*) Front View

Moving towards the tip of the riblet valleys, a motion is induced in the clockwise direction if the axis is assumed to lie along the riblet passage and the motion is viewed from the Divergent Line to the Convergent Line. The initiation of this motion can be observed from a height of $h^+ = 0.4\ h$ (where $h = 2.4$mm is the riblet height). The motion of the high momentum flow above the riblet passage helps sustain the helicoidal motion.

5.4   Effect of Reynolds Number

We obtained the results of velocity distribution along cross-stream direction at different lengths of distance from the riblet origin and the characteristics of flow over the Convergent and the Divergent Lines. Also, we analyzed the motion of the fluid inside the riblet valleys. We observed that our results were consistent with the experimental and numerical data previously worked on. Thus, building on the previous works, we aim to investigate the effects of the Reynolds Number on the flow characteristics.

From the results we obtained, it can be inferred that the strength of vorticity increases with increasing Reynolds Number. For a flow with fixed Reynolds Number, the circulation increased with longitudinal distance from the initiation of the riblet section

In the case of $Re = 10^3$, the velocity streamlines seem to be pretty straight in the vertical direction with minimal swirl motion. At consecutive Reynolds Numbers,

a weak vortex seems to be formed just above the riblet valley. For $Re = 10^3$, at a longitudinal distance of $x = 0.06m$, the center of the primary vortex lies in the region of $y^+ \approx 0.075$ (where $y^+ = y/\delta_s$; δ_s being the local boundary layer thickness).

Table 5.1: Reynolds Number vs. Vertex Center Distance at $x = 0.06m$

Reynolds Number	10^3	10^4	5×10^4	7.5×10^4
Vortex Center (y^+)	0.07	0.13	0.18	0.21

The center distances of the primary vortex for different Reynolds Numbers at a longitudinal distance of $x = 0.06m$ have been tabulated in **Table. 4.1**, which shows that as the Reynolds Number increases, the vortex shifts upwards.
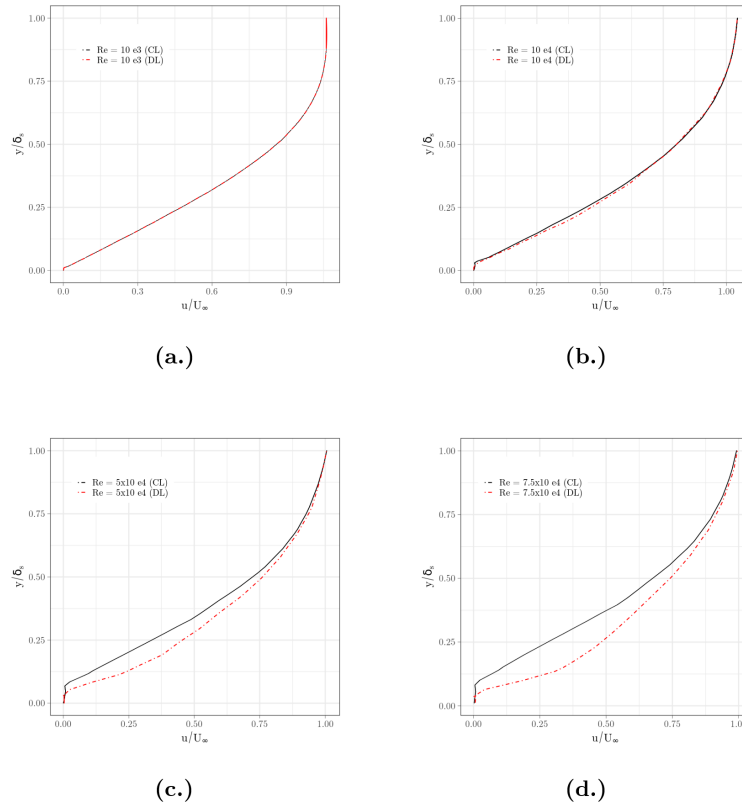

Figure 5.10: Variation of normalized longitudinal velocity against normalized wall distance at $x = 0.045m$. *(a.) $Re = 10^3$, (b.) $Re = 10^4$, (c.) $Re = 5 \times 10^4$, and (d.) $Re = 7.5 \times 10^4$*

The directional influence of the Convergent and Divergent Lines have been depicted in **Fig. 4.10**. For $Re = 10^3$, it is observable that the riblets' directional arrangement

does not impact the velocity profiles to a great extent. In fact, the velocity profiles at both lines overlap.

As the Reynolds Number increases to $Re = 10^4$, there's a slight deviation of velocity profiles at both lines for the values of $y/\delta_s \approx 0.1 - 0.75$. The velocity curves converge again afterward.

A significant deviation starts to appear for $Re = 5 \times 10^4$. The velocity profiles begin to differ from the wall itself and only converge towards the end of the local boundary layer, $y/\delta s \approx 1$.

The deviation between the velocity profiles at the two directional lines enlarges with the Reynolds Number and is maximum in the case of $Re = 7.5 \times 10^4$.
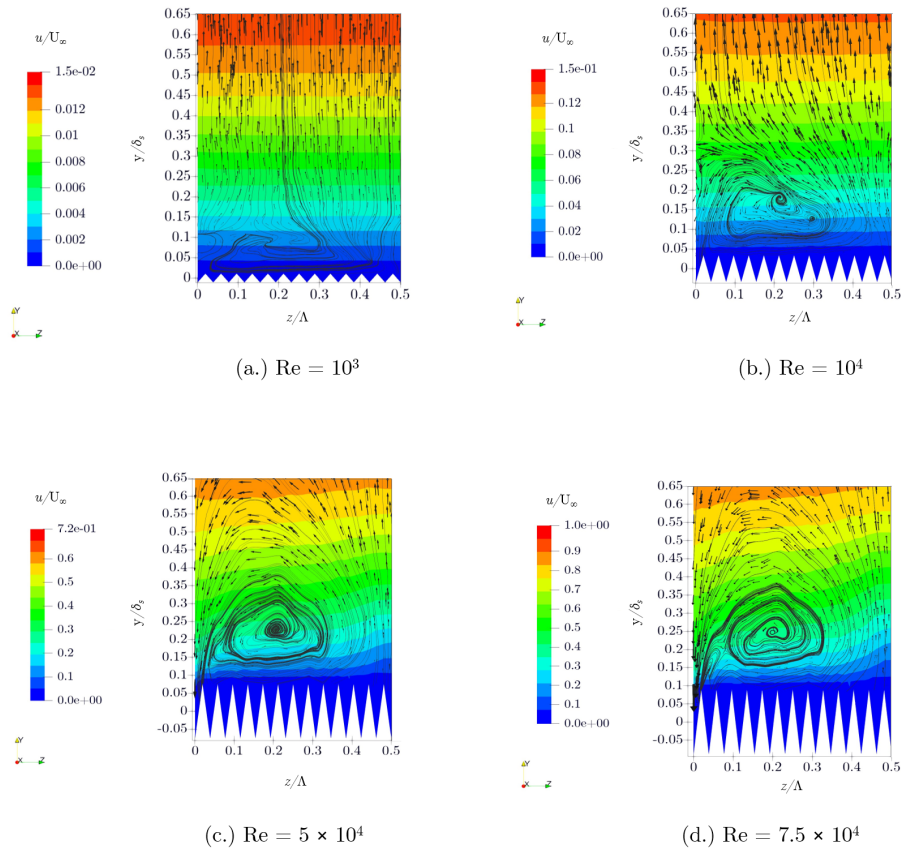

(a.) Re = 10^3

(b.) Re = 10^4

(c.) Re = 5 × 10^4

(d.) Re = 7.5 × 10^4

Figure 5.11: Representation of the induced Roll Motion in relation with increasing Reynolds Number $x = 0.045m$

The streamline patterns explain the relationship between the velocity profiles and wall-normal distance presented before. The rolling vortex seems to be in its infancy stage at the Reynolds Number of $Re = 10^3$ and much closer to riblet valleys as well as the Diverging Line.

It starts to drift upwards in the vertical stream direction with the intensity of roll

motion pitching up. As is observable in the planar velocity glyphs, the spanwise roll motion induced gets spread up to the upper edge in the case of $Re = 10^3$ and more.

The motion of the rolling vortex also seems to shift more toward the Convergent Line and an extended bulge of stationary fluid can be noticed right above the Convergent Line. The profile remains symmetrical about the Convergent Line with an opposite sense of rotation in the other half.

5.5 Conventional and Yawed Riblets

In the previous sections, the description of the boundary layer flow characteristics over a Converging-Diverging riblet section revealed the basic flow features that characterize the secondary flow induced in the spanwise direction by the directional grooves.

We now look forward to developing a comparison between the more conventional longitudinal riblets, riblets with directional grooves installed at a certain yaw angle, and transverse riblets.

Essentially, a longitudinal riblet section can be thought of as a yawed riblet with 0 yaw angle, i.e., $\gamma = 0^o$. Similarly, the transverse riblets have a yaw angle of 90°, i.e., $\gamma = 90^o$.

The value of the yaw angle for the Convergent - Divergent Riblets is kept the same as previously, i.e., $\gamma = 30^o$. The riblet height and width for all three yaw angles are the same, $s = 3.0mm$, and $h = 2.4mm$.

The difference between how these riblet configurations influence the secondary flow in a laminar boundary layer is discussed next. To begin with, we create a clipped section extending from $x = 0.675m$ from the leading edge of the plate to $x = 0.715m$ from the same. The section is extended only up to half wavelength since the nature of symmetricity of flow in the case of Convergent-Divergent Riblet and the uniformity in the spanwise direction in the case of the other two.

The velocity magnitude field suggests that the dominant component of the velocity field is the velocity in x direction, since in all three cases, the magnitude of u_x contributes the most.

Thus, it is beneficial to analyze the spanwise planar velocity in greater detail. Therefore, the glyphs have been oriented in the direction of y-z plane. **(Fig. 4.12)**

For Longitudinal Riblets, the glyphs are seemingly vertical for a large portion at the front of the section. Only a slight spanwise motion is induced at the end of the section indicating the gradual development of weak secondary flow as longitudinal distance increases.
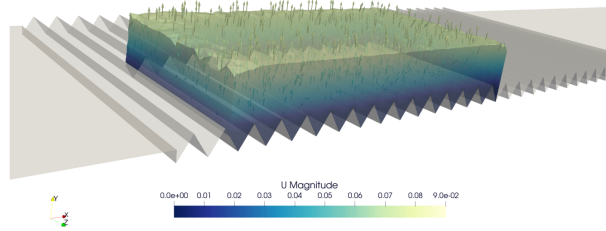
The same can be said about the transverse riblets, where the planar velocity glyph patterns seem vertically upwards and only very weak swirls are generated between the middle and the end of the section.
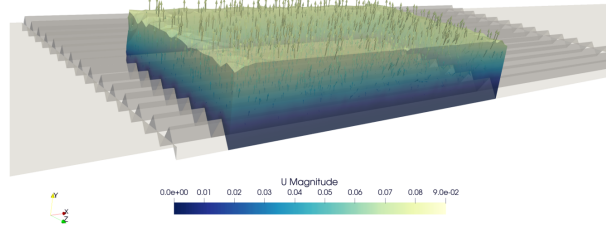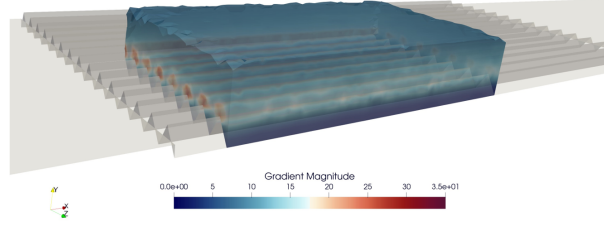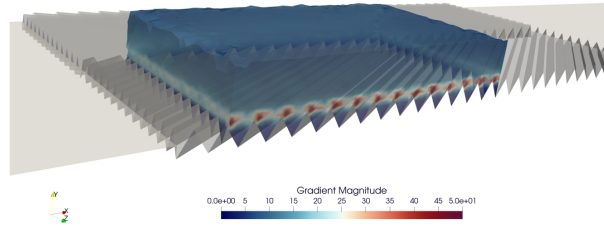

(a.)
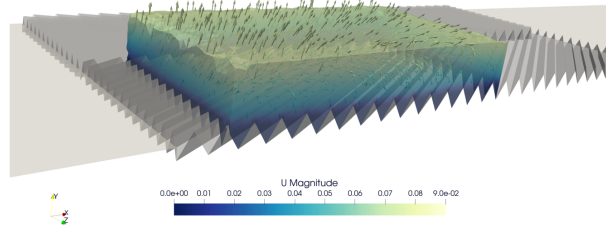
(b.)

(c.)

Figure 5.12: Sectional view of Velocity Field over : *(a.) Longitudinal Riblets, (a.) Converging-Diverging Riblets*, and *(c.) Transverse Riblets*

In the case of Converging-Diverging riblets, a significant amount of development of secondary flow can be seen developing from the start of the section itself and thus the directional pattern of grooves suggests that spanwise motion is induced to a greater effect for $0^o < \gamma < 90^o$
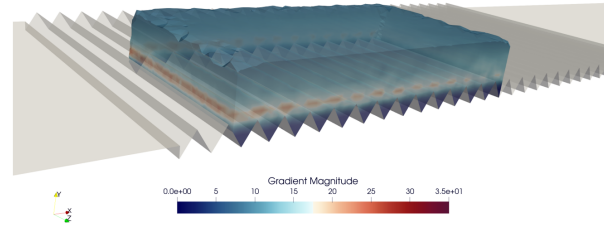
The distribution of the velocity gradient is visualized next **(Fig. 4.13)**. We can see that as was discussed earlier in the literature review, the riblets trap fluid in the space between them. The fluid in the spaces is stationary and even if the total wetted area due to the riblet sections is increased, the velocity gradient at the

(a.)

(b.)


(c.)

Figure 5.13: Sectional view of Velocity Gradient Magnitude for : *(a.) Longitudinal Riblets, (a.) Converging-Diverging Riblets*, and *(c.) Transverse Riblets*

walls is reduced to a greater extent and in the case of laminar flow, the wall shear stresses are proportional to the wall-normal gradients.

The velocity gradient at the tips of longitudinal riblets is maximum but the area of
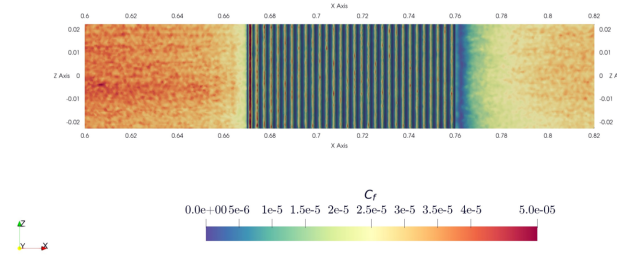
contact of these riblet tips is very small. Similarly, the accumulation of maximum velocity gradient is aligned over riblet tips in the direction of the passage of riblet tips in both C-D Riblets and Transverse Riblets.
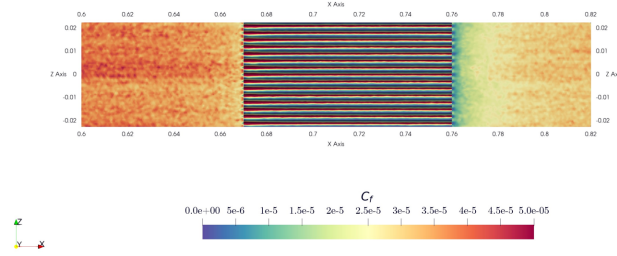
(a.)
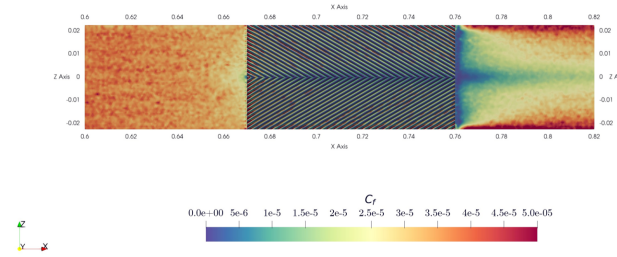
(b.)

(c.)

Figure 5.14: Coefficient of Friction : *(a.) Longitudinal Riblets*, *(a.) Converging-Diverging Riblets*, and *(c.) Transverse Riblets*

The pattern of skin friction pattern on the wall section described the effect of riblet section in both upstream and downstream directions quantitatively. **(Fig. 4.14)** Observing the section of the smooth plate just left of the riblet section, it can be deduced that the transverse riblet sections influence even the incoming flow in terms of reducing the friction drag.

In the section comprising the riblets, the pattern of the skin friction remains the

same along the passage of the riblets except for C-D riblets where, as the passage is transversed along the directional alignment, the skin friction gets reduced from the divergent line to the convergent line.

The pattern of skin friction in the section of flat plate downstream of the riblet passage is also affected by the presence of riblets. In the case of longitudinal riblets, the coefficient of friction is minimum along the length of the riblet tip, quite the opposite of the behavior from the riblet section.

The case of C-D riblets exhibits an interesting pattern over the walled surface. In the front of the riblet section line, a circular zone along the Convergent Line with a low friction coefficient is present. Over the rest of the length along the riblet wavelength, the patterns are uniform. The existence of low skin friction continues over the Convergent Line with alternate regions of high and low skin friction along riblet tips and valleys moving towards the Divergent Line. The area downstream of the riblet section exhibits two patterns. Just at the end of the section, the skin friction is minimal along the length of the riblet wavelength. The values remain similar along the Convergent line moving downstream but along the Divergent Line, it drastically increases. This behavior can be because of the spanwise motion of the rolling vortex that persists for a certain distance even if the riblet section terminates. The center of the vortex shifted towards the Diverging Line with increasing longitudinal distance after the riblet section.
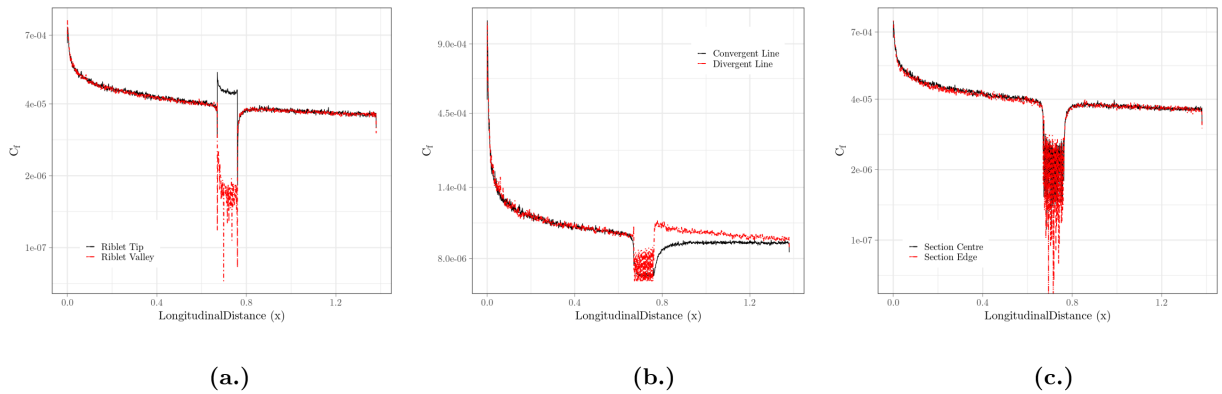
Figure 5.15: Longitudinal Variation of Skin Friction Coefficient: *(a.) Longitudinal Riblets*, *(a.) Converging-Diverging Riblets*, and *(c.) Transverse Riblets*

We conclude the results of the effect of yaw configurations with the analysis of the longitudinal distribution of Skin Friction along the characteristic wavelength distance (**Fig. 4.15**).

In Longitudinal Riblets, we see that along the length of the Riblet Tip, the value of Skin Friction increases while along the Riblet valley, it decreases.

In the case of the other two configurations, the reduction in the Skin Friction is similar along both lines, i.e., Convergent and Divergent Lines for C-D Riblets and Riblet Wavelength Section Center and Edge for transverse riblets.

Another observation is the verification of the nature of skin friction downstream of the riblet section. In the case of Longitudinal and Transverse Riblets, the Skin Friction Coefficient regains its normal curvature as it would have been without the presence of the riblet sections.

In the case of C-D riblets, the effect of the presence of the riblet section is visible even after the end of the riblets. While along the Convergent Line, the skin friction stays less, it increases along the Divergent Line.

6
Conclusion

The study was conducted to validate the results of the investigation of flow properties for the flow over the Convergent-Divergent riblets section installed on the smooth plate at a certain distance downstream of the leading edge of the flat plate using OpenFoam. The results were consistent with the experimental data and computational simulation.

Owing to this, the details of flow behavior in the boundary layer were first analyzed, and using the same simulation configuration, results were obtained for different Reynolds Numbers. It was found that the effect of Converging-Diverging riblets on the pattern of stream-wise flow was prevalent at high Reynolds Numbers in the range of near-critical values.

Next, we tried to analyze the mechanism of drag reduction by riblets with different yaw configurations and investigate the effect of these on the distribution of the skin friction coefficient over walled surfaces. It can be concluded that the effect of spanwise motion is sustained even after the end of the riblet section in the case of Convergent-Divergent Riblets.

Bibliography

[1] Xu, Fang, Shan Zhong, and Shanying Zhang. "Vortical structures and development of laminar flow over convergent-divergent riblets." Physics of Fluids 30.5 (2018).

[2] Guo, Tongbiao, Shan Zhong, and Tim Craft. "Secondary flow in a laminar boundary layer developing over convergent-divergent riblets." International Journal of Heat and Fluid Flow 84 (2020): 108598.

[3] Koeltzsch, K., A. Dinkelacker, and R. Grundmann. "Flow over convergent and divergent wall riblets." Experiments in fluids 33.2 (2002): 346-350.

[4] Bliamis, Chris, et al. "Numerical Evaluation of Riblet Drag Reduction on a MALE UAV." Aerospace 9.4 (2022): 218.

[5] Catalano, Pietro, et al. "Effects of riblets on the performances of a regional aircraft configuration in NLF conditions." 2018 AIAA Aerospace Sciences Meeting. 2018.

[6] Walsh, Michael J. "Riblets as a viscous drag reduction technique." AIAA journal 21.4 (1983): 485-486.

[7] Bechert, D. W., et al. "Experiments on drag-reducing surfaces and their optimization with an adjustable geometry." Journal of fluid mechanics 338 (1997): 59-87.

[8] Soleimani, Shima, and Steven Eckels. "A review of drag reduction and heat transfer enhancement by riblet surfaces in closed and open channel flow." International Journal of Thermofluids 9 (2021): 100053.

[9] Chen, Huawei, et al. "Flow over bio-inspired 3D herringbone wall riblets." Experiments in fluids 55 (2014): 1-7.

[10] Sharma, Vikas, and Sushanta Dutta. "Investigation of Bio-inspired Sawtooth Riblets for Boundary Layer Flow Over a Flat Surface." Iranian Journal of Science and Technology, Transactions of Mechanical Engineering (2023): 1-19.

[11] Lv, Hongqing, et al. "The Influence of boundary layer caused by riblets on the aircraft surface." Applied Sciences 10.11 (2020): 3686.

[12] Guo, Tongbiao. The effect of convergent-divergent riblets on laminar wall-bounded flows. Diss. University of Manchester, 2021.

[13] Von Deyn, Lars H., Davide Gatti, and Bettina Frohnapfel. "From drag-reducing riblets to drag-increasing ridges." Journal of Fluid Mechanics 951 (2022): A16.

[14] Bechert, D. W., and W. Hage. "Drag reduction with riblets in nature and engineering." WIT Transactions on State-of-the-art in Science and Engineering 4 (2006).

[15] Stübing, D., and H. Kordy. "Riblet-surfaces for improvement of efficiency of wind turbines." D10 2.

[16] García-Mayoral, Ricardo, and Javier Jiménez. "Drag reduction by riblets." Philosophical transactions of the Royal society A: Mathematical, physical and engineering Sciences 369.1940 (2011): 1412-1427.

[17] Chamorro, Leonardo P., R. E. A. Arndt, and Fotis Sotiropoulos. "Drag reduction of large wind turbine blades through riblets: Evaluation of riblet geometry and application strategies." Renewable Energy 50 (2013): 1095-1105.

[18] Jovičić, N., Michael Breuer, and J. Jovanović. "Anisotropy-invariant mapping of turbulence in a flow past an unswept airfoil at high angle of attack." (2006): 559-567.

[19] https://rest.neptune-prod.its.unimelb.edu.au/server/api/core/bitstreams/78bd6cf6-49c8-5c53-85ff-e6e9ba2b5dd9/content

[20] Grüneberger, René, and Wolfram Hage. "Drag characteristics of longitudinal and transverse riblets at low dimensionless spacings." Experiments in Fluids 50 (2011): 363-373.

[21] Viswanath, P. R. "Aircraft viscous drag reduction using riblets." Progress in Aerospace Sciences 38.6-7 (2002): 571-600.

[22] Zhang, Yang, et al. "Numerical analysis of turbulence characteristics in a flat-plate flow with riblets control." Advances in Aerodynamics 4.1 (2022): 1-28.

[23] Frohnapfel, Bettina, et al. "Interpretation of the mechanism associated with turbulent drag reduction in terms of anisotropy invariants." Journal of Fluid Mechanics 577 (2007): 457-466.

[24] Garcia-Mayoral, Ricardo, and Javier Jimenez. "Hydrodynamic stability and breakdown of the viscous regime over riblets." Journal of Fluid Mechanics 678 (2011): 317-347.

[25] Bechert, D. W., and M. Bartenwerfer. "The viscous flow on surfaces with longitudinal ribs." Journal of fluid mechanics 206 (1989): 105-129.